

## Durham Research Online

---

### Deposited in DRO:

28 August 2018

### Version of attached file:

Accepted Version

### Peer-review status of attached file:

Peer-reviewed

### Citation for published item:

Lucier, Bryan E. G. and Johnston, Karen E. and Arnold, Donna C. and Lemyre, Jean-Luc and Beaupré, Ariane and Blanchette, Maxime and Ritcey, Anna M. and Schurko, Robert W. (2013) 'Comprehensive solid-state characterization of rare earth fluoride nanoparticles.', *Journal of physical chemistry C*, 118 (2). pp. 1213-1228.

### Further information on publisher's website:

<https://doi.org/10.1021/jp408148b>

### Publisher's copyright statement:

This document is the Accepted Manuscript version of a Published Work that appeared in final form in *Journal of physical chemistry C* copyright © American Chemical Society after peer review and technical editing by the publisher. To access the final edited and published work see <https://doi.org/10.1021/jp408148b>

### Additional information:

---

### Use policy

The full-text may be used and/or reproduced, and given to third parties in any format or medium, without prior permission or charge, for personal research or study, educational, or not-for-profit purposes provided that:

- a full bibliographic reference is made to the original source
- a [link](#) is made to the metadata record in DRO
- the full-text is not changed in any way

The full-text must not be sold in any format or medium without the formal permission of the copyright holders.

Please consult the [full DRO policy](#) for further details.

# Comprehensive Solid-State Characterization of Rare Earth Fluoride Nanoparticles

Bryan E.G. Lucier,<sup>1</sup> Karen E. Johnston,<sup>1</sup> Donna C. Arnold,<sup>2</sup>

Jean-Luc Lemyre,<sup>3</sup> Ariane Beaupré,<sup>3</sup> Maxime Blanchette,<sup>3</sup>

Anna M. Ritcey,<sup>3</sup> and Robert W. Schurko<sup>1,\*</sup>

<sup>1</sup> *Department of Chemistry and Biochemistry, University of Windsor,  
Windsor, Ontario, Canada, N9B 3P4*

<sup>2</sup> *University of Kent, School of Physical Sciences, Canterbury, Kent, United Kingdom, CT2 7NH*

<sup>3</sup> *Department of Chemistry and CERMA, Université Laval, Québec, Canada, G1V 0A6*

\* To whom correspondence should be addressed.

Phone: 519-253-3000 x3548 Fax: 519-973-7098, E-mail: [rschurko@uwindsor.ca](mailto:rschurko@uwindsor.ca)

## Abstract

The combination of multinuclear solid-state NMR and powder X-ray diffraction has been applied to characterize the octahedron-shaped crystalline nanoparticle products resulting from an inverse micelle synthesis. Rietveld refinements of the powder X-ray diffraction data from the nanoparticles reveal their general formula to be  $(\text{H}_3\text{O})\text{Y}_3\text{F}_{10} \cdot x\text{H}_2\text{O}$ .  $^1\text{H}$  magic-angle spinning (MAS) NMR experiments provide information on sample purity, as well as serving as an excellent probe of the zeolithic incorporation of atmospheric water.  $^{19}\text{F}$  MAS NMR experiments on a series of monodisperse nanoparticle samples of various sizes yield spectra featuring three unique  $^{19}\text{F}$  resonances, arising from three different fluorine sites within the  $(\text{H}_3\text{O})\text{Y}_3\text{F}_{10} \cdot x\text{H}_2\text{O}$  crystal structure. Partial removal of zeolithic water from the internal cavities and tunnels of the nanoparticles leads to changes in the integrated peak intensities in the  $^{19}\text{F}$  MAS NMR spectra; the origin of this behaviour is discussed in terms of  $^{19}\text{F}$  longitudinal relaxation.  $^{19}\text{F}$ - $^{89}\text{Y}$  variable-amplitude cross-polarization (VACP) NMR experiments on both stationary samples and samples under conditions of MAS indicate that two distinct yttrium environments are present, and based on the relative peak intensities, the populations of one of the two sites is closely linked to nanoparticle size. Both  $^{19}\text{F}$  MAS and  $^{19}\text{F}$ - $^{89}\text{Y}$  VACP/MAS experiments indicate small amounts of an impurity present in certain nanoparticles; these are postulated to be spherical amorphous  $\text{YF}_3$  nanoparticles. We discuss the importance of probing molecular-level structure in addition to microscopic structure, and how the combination of these characterization methods is crucial for understanding nanoparticle design, synthesis, and application.

**Keywords:** nanoparticles, zeolite, solid-state NMR, powder X-ray diffraction,  $^{19}\text{F}$  NMR,  $^{89}\text{Y}$  NMR, characterization

## Introduction

Nanoparticles (NPs), small clusters of atoms with dimensions on the order of  $10^{-9}$  to  $10^{-7}$  m, exhibit a wide array of unique properties not observed in bulk materials. As such, NPs are intensively studied, in large part due to their potential applications in bioimaging, drug delivery, and optics.<sup>1-6</sup> Many NPs contain rare earth<sup>7-9</sup> and lanthanide<sup>10-19</sup> elements, which are important for their contributions to the composition and structural makeup of the NP, as well as novel physicochemical behaviour (*e.g.*, enhanced optical properties). Recently, the preparation of yttrium fluoride ( $\text{YF}_3$ )-based NPs *via* an inverse micelle process was reported,<sup>20,21</sup> with an exceptional level of control exhibited over the size, shape, and crystallinity of the final products. These NPs have octahedral shapes, and their electron diffraction patterns do not match that of bulk  $\text{YF}_3$ , indicating that different solid phases are formed during their synthesis.<sup>20</sup> The combination of physical (size, shape) and chemical (phase, crystallinity) control over the product afforded by this NP synthesis naturally presents a variety of possible applications for rare earth and **lanthanide** fluoride-based NPs.<sup>22-28</sup>

NPs are typically characterized by electron microscopy and UV-Vis spectroscopy. The former technique yields information regarding the size and morphology of NPs, whereas the latter sheds light upon the molecular/atomic origins of optical properties. Powder X-ray diffraction (pXRD) methods are also often used to characterize crystalline NPs and offer the opportunity for determination of the crystal space group, and in some cases, the unit cell parameters and associated crystal structure.<sup>29-39</sup> In the case of partially or fully amorphous NPs, pXRD can provide some useful data regarding crystallinity and NP size, but information pertaining to the long-range structure and atomic bonding/interactions is generally unavailable.

Solid-state nuclear magnetic resonance (SSNMR) experiments are often employed to study NPs, providing information on the molecular-level structure,<sup>40-44</sup> short- and long-range order,<sup>45-48</sup> core/shell interfaces,<sup>49-52</sup> ligand/NP interactions,<sup>53-57</sup> and dopants.<sup>58-61</sup> In particular,  $^1\text{H}$  and  $^{13}\text{C}$  SSNMR experiments are routinely applied to study the nature of stabilizing organic surface ligands on inorganic NPs. The structures of NPs with inorganic cores can be further probed if there are nuclides present that are amenable to study by NMR spectroscopy.  $^{19}\text{F}$  and  $^{89}\text{Y}$  are both spin-1/2 nuclei, 100% naturally abundant, and possess moderate chemical shift ranges.  $^{19}\text{F}$  is highly receptive,<sup>62,63</sup> whereas  $^{89}\text{Y}$  is unreceptive due to its low gyromagnetic ratio. Furthermore,  $^{89}\text{Y}$  SSNMR experiments utilizing direct excitation suffer from poor signal-to-noise ratios (S/N), due not only to the low  $\gamma$ , but also to typically lengthy longitudinal relaxation times ( $T_1(^{89}\text{Y})$ );<sup>64</sup> hence,  $^{89}\text{Y}$  NMR spectra are often acquired using cross-polarization (CP) methods.

Herein, we present a comprehensive SSNMR and pXRD study of crystalline  $\text{YF}_3$ -based NPs, in order to study the NP composition as well as the molecular-level structures of their cores and surfaces. Powder XRD experiments and Rietveld refinements are used to identify the structure of the unknown phase of the crystalline octahedral NPs.  $^{89}\text{Y}$  and  $^{19}\text{F}$  SSNMR experiments on NPs of varying size are utilized to examine the unique Y and F environments, and the corresponding NMR resonances are correlated to crystallographic sites.  $^1\text{H}$  and  $^{19}\text{F}$  NMR experiments are used to probe the interactions between water molecules and the NP surfaces, and  $^1\text{H}$  and  $^{13}\text{C}$  NMR are used to study the stabilizing surface ligands. Finally, we discuss the value of an intimate knowledge of NP structure and composition, and its relation to synthetic methods and starting materials, which is essential for the future rational design of NPs with controllable and tunable bulk properties.

## Experimental

**Synthesis of single crystal  $(\text{H}_3\text{O})\text{Y}_3\text{F}_{10} \cdot x\text{H}_2\text{O}$  nanoparticles.** All chemicals were supplied by Sigma Aldrich and used without further purification. Octahedral NPs of different sizes were prepared using variations of a previously described method.<sup>20</sup> The general procedure consists of the addition of aqueous fluoride to a solution of  $\text{YCl}_3$  dispersed within reverse micelles, which frequently results in a mixture of particle populations that differ in shape or crystallinity. In order to facilitate spectral analysis, synthetic conditions were selected so as to maximize the production of a uniform population of monodisperse octahedral  $(\text{H}_3\text{O})\text{Y}_3\text{F}_{10} \cdot x\text{H}_2\text{O}$  NPs. The reagent quantities are reported as absolute values, rather than concentrations, because the resultant particle size depends slightly on the overall volume of solution (Table 1). NPs doped with 5% scandium were also prepared (Supporting Information, Figure S1). For each sample, reverse microemulsions were prepared by mixing an aqueous solution of  $\text{YCl}_3$ , cyclohexane and the surfactants polyoxyethylene(5)nonylphenylether (Igepal CO520) and sodium bis(2-ethylhexyl)sulfosuccinate (AOT). Microemulsions were homogenized with a magnetic stirrer followed by 10 minutes in an ultrasonic bath. An aqueous solution of  $\text{NH}_4\text{HF}_2$  was then added directly to the microemulsion, with vigorous stirring under ambient conditions. Stirring was maintained over a week to ensure completion of particle growth. The resulting suspensions of  $(\text{H}_3\text{O})\text{Y}_3\text{F}_{10} \cdot x\text{H}_2\text{O}$  nanocrystals appeared clear and were deposited directly on TEM grids. NPs for NMR analysis were isolated from the microemulsions by evaporation of the cyclohexane, dissolution in methanol and centrifugation. Soluble counterions and surfactants were removed by four dispersion/centrifugation cycles using water alternately with methanol. The precipitated NPs were then allowed to dry overnight in an oven at a temperature of 90 °C. The resulting white powders were used for NMR measurements.

**Table 1.** Synthetic parameters for  $(\text{H}_3\text{O})\text{Y}_3\text{F}_{10} \cdot x\text{H}_2\text{O}$  nanoparticle samples.

Particle Size (nm) <sup>a</sup>	Cyclohexane Volume (mL)	Igepal Mass (g)	AOT Mass (g)	Aqueous Volume <sup>b</sup> (mL)	$[\text{YCl}_3(\text{aq})]$ <sup>c</sup> (mmol/L)
21	450	60	-	12	40
37	450	54	6	15	40
67	90	10.8	1.2	3	500
132 <sup>d</sup>	90	3	-	3	500
49	450	54	6	15	38 <sup>e</sup>
83	300	36	4	10	400

<sup>a</sup> The octahedral particle sizes reported in this paper refer to length of the octahedron edge. See text for details. <sup>b</sup> The volume of aqueous  $\text{NH}_4\text{HF}_2$  added to the microemulsion equals the volume of the aqueous solution of  $\text{YCl}_3$  initially present. <sup>c</sup>  $[\text{NH}_4\text{HF}_2(\text{aq})] = [\text{YCl}_3(\text{aq})]$  <sup>d</sup> Sample prepared at 8 °C, all others at room temperature. <sup>e</sup> 2 mmol/L  $\text{ScCl}_3$  was added to the initial aqueous solution to obtain  $\text{YF}_3\text{:Sc}$  5% doped nanoparticles.

A separate batch of 83 nm  $(\text{H}_3\text{O})\text{Y}_3\text{F}_{10} \cdot x\text{H}_2\text{O}$  NPs were synthesized in order to study the effects of sample hydration on  $^{89}\text{Y}$  NMR spectra; these SSNMR experiments were performed after experiments on all of the other NP particles had been conducted, as earlier samples (*i.e.*, 21, 37, 49, 67 and 132 nm NPs) were not present in sufficient quantities for continued NMR experimentation. Experimental parameters related to the synthesis of these 83 nm NPs are listed in Table 1. The 83 nm NPs do not appear in any portions of this work aside from  $^{19}\text{F}$ -  $^{89}\text{Y}$  NMR experiments.

TEM images and electron diffraction patterns were recorded with a JEOL JEM-1230 at an accelerating voltage of 120 kV. Samples were prepared by allowing a drop of the  $(\text{H}_3\text{O})\text{Y}_3\text{F}_{10} \cdot x\text{H}_2\text{O}$  suspensions, as obtained by the syntheses described above, to dry directly on a carbon coated nickel microscope grid, leaving a significant amount of octahedrally-shaped  $(\text{H}_3\text{O})\text{Y}_3\text{F}_{10} \cdot x\text{H}_2\text{O}$  nanoparticles<sup>20</sup> for observations. Size measurements were made on randomly selected particles with

the Scion Image software. Since TEM provides two-dimensional projections, these octahedral nanoparticles appear as hexagons, squares, or rhombuses, depending on their orientation on the TEM grid. Particle size was not measured from two opposite corners of the observed hexagons because these two points are not in the same plane and the length measured would therefore be inaccurate. Instead, the measurements were made between two adjacent corners which correspond to an actual octahedron edge. The octahedral particle sizes reported in this paper refer to length of the octahedron edge. Figure 1 shows TEM images of the  $(\text{H}_3\text{O})\text{Y}_3\text{F}_{10} \cdot x\text{H}_2\text{O}$  NPs. All samples in this study feature a single population of monodisperse NPs, except for the 21 and 132 nm sample, for which small numbers of spherical amorphous particles and triangular prism particles are also observed via TEM. No synthetic conditions were found that allowed for the complete elimination of these secondary particle populations.

**Powder X-ray diffraction.** Powder XRD (pXRD) experiments were performed on a Bruker AXS HI-STAR system using a General Area Detector Diffractions system with a  $\text{Cu K}_\alpha$  ( $\lambda = 1.54056$  Å) radiation source. Simulations of pXRD patterns from known crystal structures<sup>65</sup> were performed using PowderCell.<sup>66</sup> Rietveld refinements<sup>67</sup> of the 67 nm diameter NPs were completed using the Fullprof suite of programs.<sup>68,69</sup> **Refinements were conducted for 47 variables, including 34 background coefficients fitted using a linear interpolation function, detector zero point (0.06704), lattice parameters and profile coefficients fitted using a Thomson-Cox-Hastings function.<sup>70</sup> However, due to the abundance of light atoms within the proposed structural model and the quality of the pXRD data it was not appropriate to refine the individual atomic thermal parameters of the system. Further information on the refinement parameters is provided in Appendix A of the Supporting**



**Information.** The structures shown in Figure 4 were generated using the parameters obtained from Rietveld refinement of the pXRD data and the Vesta<sup>71</sup> software program.

**Solid-State NMR.** Solid-state NMR spectra were collected on a Varian Infinity Plus NMR spectrometer with an Oxford 9.4 T ( $\nu_0(^1\text{H}) = 399.73$  MHz) wide-bore magnet with  $\nu_0(^{19}\text{F}) = 376.73$  MHz and  $\nu_0(^{89}\text{Y}) = 19.69$  MHz.  $^1\text{H}$  and  $^{19}\text{F}$  magic-angle spinning (MAS) experiments were performed using a Varian/Chemagnetics 2.5 mm HX probe. All  $^{89}\text{Y}$  experiments, both static (non-spinning) and MAS, were conducted using a Varian/Chemagnetics 4 mm HXY probe. A Chemagnetics low- $\gamma$  tuning box and preamplifier were used on the X channel for all  $^{89}\text{Y}$  NMR experiments. All samples were packed into 2.5 mm or 4 mm o.d. zirconia rotors.  $^1\text{H}$  chemical shifts were referenced to tetramethylsilane (TMS,  $\delta_{\text{iso}} = 0.0$  ppm) using adamantane ( $\delta_{\text{iso}} = 1.85$  ppm) as a secondary reference.  $^{19}\text{F}$  chemical shifts were referenced with respect to neat  $\text{CFCl}_3$  (l) ( $\delta_{\text{iso}} = 0.0$  ppm) using Teflon ( $(\text{C}_2\text{F}_4)_n$ ,  $\delta_{\text{iso}} = -122.0$  ppm) as a secondary reference.  $^{89}\text{Y}$  chemical shifts were referenced to a 1.0 M  $\text{YCl}_3$  (aq) solution ( $\delta_{\text{iso}} = 0.0$  ppm).  $^{45}\text{Sc}$  experiments were attempted; however, the spectra were found to be uninformative, and are not discussed further in this work.

$^1\text{H}$  NMR spectra were acquired at a spinning speed of 25 kHz using a standard Bloch decay pulse sequence, with a  $\pi/2$  pulse width of 3.0  $\mu\text{s}$ , spectral width of 100 kHz and recycle delay of 5 s. The spectrum of an empty rotor containing Teflon tape (used to fill the space between the cap and the sample) was used to correct experimental spectra for background signal, of which there was little (Figure S2). See Table S1 of the Supporting Information for additional  $^1\text{H}$  experimental parameters.  $^{19}\text{F}$  MAS NMR spectra were acquired at a spinning speed of 25 kHz under rotor-synchronized conditions using a standard Hahn-echo experiment of the form  $(\pi/2)_x - \tau_1 - (\pi)_y - \tau_2 - \text{acq}$ , where  $\tau_1$  and

$\tau_2$  represent interpulse delays of 40 and 10  $\mu$ s, respectively. A  $^{19}\text{F}$   $\pi/2$  pulse width of 2.1  $\mu$ s and spectral width of 400 kHz were used, along with pulse delays of 5 s and 30 s to ensure complete longitudinal ( $T_1$ ) relaxation of  $^{19}\text{F}$  nuclei. Generally, at least two different spinning speeds were employed for all experiments to distinguish isotropic chemical shifts from spinning sidebands; however, only spectra with a spinning speed of 25 kHz were used for analysis due to enhanced signal and resolution of isotropic chemical shifts. See Table S2 for full listings of  $^{19}\text{F}$  NMR experimental parameters.

$^{19}\text{F}$ - $^{89}\text{Y}$  cross polarization<sup>72</sup> (CP) NMR experiments were performed using the VACP pulse sequence<sup>73,74</sup> with two-pulse phase-modulation (TPPM)  $^{19}\text{F}$  decoupling.<sup>75</sup> For these experiments,  $^{19}\text{F}$   $\pi/2$  pulse widths of 2.5  $\mu$ s were applied, with contact times from 5 to 11 ms and recycle delays of 5.0 s. Spectral widths of 40 kHz were generally used. Hartmann-Hahn matching fields of 22 kHz for  $^{19}\text{F}$  and 43 kHz for  $^{89}\text{Y}$  were used in all instances. Experiments were either conducted on static samples, or at a spinning speed of 5 kHz. A  $^{19}\text{F}$  decoupling field of 48 kHz was employed in all experiments. For complete experimental details, refer to Table S3.

Simulations of all static solid-state NMR spectra were performed using the WSOLIDS software package.<sup>76</sup> In all cases, uncertainties in the extracted NMR tensor parameters were estimated using bidirectional variation within the simulation software. The uncertainties associated with individual chemical shift tensor components ( $\delta_{11}$ ,  $\delta_{22}$  and  $\delta_{33}$ ) were calculated through propagation of error from experimental  $\delta_{\text{iso}}$ ,  $\Omega$  and  $\kappa$  values. Processing, line-fitting, and integration of spectra was performed using the NUTS software package from Acorn NMR.

## Results and Discussion

**Powder X-ray diffraction.** pXRD experiments were completed for NPs with diameters of 132, 67, and 37 nm, respectively. Bulk  $\text{YF}_3$  belongs to space group  $Pnma$ ; however, our pXRD data (Figure 2) indicate that the NPs crystallize in a different space group. This was also reported in a study by Lemyre *et al.*, in which it was found that NPs with different diameter sizes exhibited identical electron diffraction patterns that could not be indexed to the same orthorhombic symmetry as bulk  $\text{YF}_3$ .<sup>20</sup>

The pXRD data for NPs with diameters of 132, 67, and 37 nm were indexed to a cubic symmetry, in space group  $Fd-3m$ , with a lattice parameter,  $a$ , of ca. 15.5 Å. Search-match software analysis indicates that these materials adopt a diamond-like structure similar to those previously reported for  $(\text{H}_3\text{O})\text{Ln}_3\text{F}_{10} \cdot x\text{H}_2\text{O}$ , where Ln = Lu, Yb, Tm, Er or Y,<sup>77,78</sup> and  $(\text{C}_3\text{N}_2\text{H}_{12})_{0.5}\text{Y}_3\text{F}_{10}$ .<sup>79</sup> The Rietveld refinement completed for the 67 nm diameter NPs displays excellent agreement with the calculated model ( $wR_p = 3.99\%$  and  $\chi^2 = 1.14$ , Figure 3) and is consistent with previous reports.<sup>77-80</sup> Full refinement details are given in Tables 2 and 3.

**Table 2.** Structural parameters for the 67 nm  $(\text{H}_3\text{O})\text{Y}_3\text{F}_{10} \cdot 0.6\text{H}_2\text{O}$  nanoparticles.<sup>a</sup> Space group  $Fd-3m$ ,  $a = 15.4876(9)$  Å and  $V = 3715.0(4)$  Å<sup>3</sup>.  $\chi^2 = 1.14$ ,  $wR_p = 3.99$  % and  $R_p = 6.23$  %.

Atom	Site	x	y	z	Fractional Occupancy
Y	48f	0.375(2)	0.375(2)	0.0520(3)	1
<i>Fl'</i> <sup>b</sup>	96h	0	0.8641(8)	0.5	1
<i>Fl'</i>	96h	0	0.1359(8)	0.5	1
<i>F2'</i>	32	0.219(1)	0.219(1)	0.219(1)	1
<i>F3'</i>	32	0.048(1)	0.048(1)	0.048(1)	1
H <sub>3</sub> O <sup>+</sup>	16d	0.5	0.5	0.5	1
H <sub>2</sub> O	48f	0.375(2)	0.375(2)	0.321(4)	0.21(2)

<sup>a</sup> Refinement of our partially hydrated sample yielded  $x = 0.6$  with respect to the structural formula  $(\text{H}_3\text{O})\text{Y}_3\text{F}_{10} \cdot x\text{H}_2\text{O}$ , and is discussed in the text. <sup>b</sup> Fluorine labels are listed in italics with prime symbols to differentiate these atoms from those within bulk  $\text{YF}_3$ . See text for details.

**Table 3.** Relevant interatomic lengths obtained from Rietveld refinement of the 67 nm diameter  $(\text{H}_3\text{O})\text{Y}_3\text{F}_{10} \cdot 0.6\text{H}_2\text{O}$  nanoparticle pXRD pattern.

Bond	Bond Length (Å)
Y - <i>Fl'</i>	2.337(8)
Y - <i>F2'</i>	2.42(2)
Y - <i>F3'</i>	2.29(2)
<i>Fl'</i> - O	2.49(4)

The diamond-like structure exhibited by these materials (Figure 4) has been described extensively in the literature.<sup>77,79,80</sup> The yttrium ions are in eight-coordinate square antiprismatic polyhedral sites that are face shared around a distorted cubic cavity to form a larger octahedral-like  $[\text{Y}_6\text{F}_{32}]^{14-}$  building block, which is termed a unit of octahedral antiprisms (UOA). Edge- and corner-shared UOA are linked to form a three-dimensional cage-like structure, which allows for

movement of H<sub>2</sub>O molecules within cavities linked by channels. In all previous models, the inclusion of charge-balancing ions are reported. It is therefore likely that hydronium ions, as well as water molecules, are located within the void spaces of the structure. This is consistent with the model proposed for (H<sub>3</sub>O)Y<sub>3</sub>F<sub>10</sub> • xH<sub>2</sub>O in which cavities and channels are statistically populated by zeolithic water molecules, while the hexagonal-shaped cavity entry points within channels are occupied by H<sub>3</sub>O<sup>+</sup>.<sup>77,78</sup> Rietveld refinements were improved by including the O ions of H<sub>2</sub>O and H<sub>3</sub>O<sup>+</sup> species, which yielded a general formula of (H<sub>3</sub>O)Y<sub>3</sub>F<sub>10</sub> • 0.6H<sub>2</sub>O. Since the sample for pXRD was dried in an oven prior to analysis in order to drive off zeolithic H<sub>2</sub>O, a value of  $x = 0.6$  was determined, rather than the expected value of  $x = 1$  for a fully hydrated sample.<sup>78</sup> Attempts to replace the hydronium ions with ammonium ions did not improve the refinement, indicating that no residual NH<sub>4</sub><sup>+</sup> from the NH<sub>4</sub>HF<sub>2</sub> solvent used during the synthesis remains in the channels. The possibility of F vacancies and/or Cl substitution (from the starting reagent YCl<sub>3</sub>) within the (H<sub>3</sub>O)Y<sub>3</sub>F<sub>10</sub> • 0.6H<sub>2</sub>O framework cannot be discounted, although Cl substitution seems unlikely given that previous work has indicated no presence of Cl whatsoever in samples prepared via the same synthetic route.<sup>20</sup> Rietveld refinements accounting for F vacancies were attempted, but were unsuccessful.

**<sup>1</sup>H MAS NMR Experiments.** <sup>1</sup>H NMR experiments were performed to ascertain the purity of (H<sub>3</sub>O)Y<sub>3</sub>F<sub>10</sub> • xH<sub>2</sub>O NPs, as well as to investigate their uptake of water. Spectra of hydrated samples were acquired after exposure to ambient conditions for over two weeks. Previous thermogravimetric analyses and X-ray thermodiffraction studies indicate that sample decomposition to YF<sub>3</sub> is possible at high temperatures;<sup>77-79</sup> hence, to ensure partial dehydration of zeolithic H<sub>2</sub>O without decomposition of the sample or phase changes, only samples that were placed in an oven at 125 °C for at least four hours were subjected to NMR experimentation.

The  $^1\text{H}$  MAS NMR spectra of fully and partially hydrated 67 nm  $(\text{H}_3\text{O})\text{Y}_3\text{F}_{10} \cdot x\text{H}_2\text{O}$  NPs are shown in Figure 5, and information regarding individual resonances is given in Table S4. The relatively efficient longitudinal  $^1\text{H}$  relaxation allowed for fairly short pulse delays of 5 s to be employed (Figure S3). Two broad patterns are present between 4 and 7 ppm. The resonances centered at ca. 4.3 and 4.7 ppm in the spectra of the partially and fully hydrated NPs, respectively, correspond to zeolitic water; similar resonances have been observed in  $^1\text{H}$  NMR spectra of silica-, titania-, and alumina-based mesoporous solids.<sup>81-84</sup> Resonances of comparable breadths are centered at ca. 6.8 ppm for both partially and fully hydrated samples, and correspond to the  $\text{H}_3\text{O}^+$  species within the NP channels. The integrated area of the  $\text{H}_2\text{O}$  resonance compared to that of  $\text{H}_3\text{O}^+$  is 14.2 : 10.0 in the fully hydrated sample, but only 7.5 : 10.0 in the partially hydrated sample (Figures S4 and S5, Table S4), indicating that heating at temperatures of 125 °C is sufficient to at least partially eliminate zeolitic water. It should be noted that the integrated area of the  $\text{H}_2\text{O}$  resonance with respect to the  $\text{H}_3\text{O}^+$  resonance in the spectra of the fully hydrated NPs exceeds the 1:1 stoichiometry expected from a fully hydrated sample,<sup>77,78</sup> which indicates either that additional  $\text{H}_2\text{O}$  must be present in the sample, likely on the surfaces of the NPs, and/or the overlap of  $\text{H}_2\text{O}$  and  $\text{H}_3\text{O}^+$  resonances results in some uncertainty of the integrated areas.

The sharp resonances observed at 1.4 and 1.0 ppm in both spectra are due to the presence of residual sodium bis(2-ethylhexyl)sulfosuccinate (AOT) and polyoxyethylene(5)nonylphenylether (Igepal520) surfactants, respectively.<sup>85-87</sup> The differences in intensity of the resonances at 1.4 ppm between samples might be linked with the degree of sample hydration, but are likely related in part to the differences in integrated areas of the broad, overlapping adjacent  $\text{H}_2\text{O}$  resonance. The surfactants are likely present in tiny amounts, as suggested by the small integrated areas of their

resonances compared to those of  $\text{H}_2\text{O}$  and  $\text{H}_3\text{O}^+$  (Table S4). Experiments employing shorter  $^1\text{H}$  pulse delays also suggest relatively small amounts of surfactant are present (Figure S3). The surfactant is located on the exterior surface of the NP and is unlikely to occupy channels or cavities due to steric restrictions.<sup>79</sup>  $^1\text{H}$ - $^{13}\text{C}$  CP NMR experiments detect trace amounts of residual surfactant, consistent with the relatively small amounts indicated by the  $^1\text{H}$  MAS spectra. The only  $^1\text{H}$ - $^{13}\text{C}$  VACP/MAS spectrum that was obtained required an optimized contact time of 3 ms and has two broad resonances of low intensity centered at 85 and 30 ppm (Figure S6), owing to the small quantities of any surfactant present on the NP surface.

Water mobility is known to be exceptionally high within this family of compounds,<sup>77,78</sup> and the sharp resonances at ca. 0.1 ppm in Figure 5 are due to water molecules occupying the void space between  $(\text{H}_3\text{O})\text{Y}_3\text{F}_{10} \cdot x\text{H}_2\text{O}$  NPs. This resonance is more intense in the spectra of fully hydrated NPs and exhibits a chemical shift corresponding to that of highly mobile monomeric gaseous water (*i.e.*, isolated water molecules not interacting with surroundings).<sup>88,89</sup> It is possible that a resonance with this chemical shift could arise from surface hydroxyl species bound to metals<sup>83,90,91</sup> (in this case yttrium); however, this is unlikely, since the  $^1\text{H}$  linewidths are too narrow to correspond to surface-bound groups, the NP crystal structure indicates exterior surfaces should largely consist of fluorine, and any surface hydroxyl species would have to arise from uncommon defect sites. Our Rietveld refinements (*vide supra*) and  $^{19}\text{F}$  MAS NMR experiments (*vide infra*) also indicate no significant level of F vacancies or substitutions in the  $(\text{H}_3\text{O})\text{Y}_3\text{F}_{10} \cdot x\text{H}_2\text{O}$  NPs.  $^1\text{H}$  MAS NMR experiments confirm the purity (*i.e.*, only the expected surface species and water molecules are present) and zeolitic structure of the NPs, but cannot provide any further information on their

molecular-level structure and composition. In order to investigate the structure within the inorganic NP cores,  $^{19}\text{F}$  and  $^{89}\text{Y}$  SSNMR experiments must be considered.

**$^{19}\text{F}$  MAS NMR Experiments.** The crystal structure of bulk  $\text{YF}_3$ , which has a space group of *Pnma*, indicates that there is a unique yttrium site which is coordinated by nine fluorine atoms (Figure 6). There are two crystallographically distinct fluorines, **F1** and **F2**, which exist in a ratio of 1:2. The  $^{19}\text{F}$  MAS NMR spectrum of bulk  $\text{YF}_3$  reveals two sharp resonances with distinct chemical shifts and relative integrated intensities of 2:1 (Figure 7(a)); hence, peaks at -56 and -67 ppm are assigned to **F2** and **F1**, respectively. Both resonances are also associated with spinning sideband manifolds, which under conditions of fast MAS, may be utilized to extract information on the fluorine CS tensors (*vide infra*).

$^{19}\text{F}$  MAS NMR experiments were also performed on  $(\text{H}_3\text{O})\text{Y}_3\text{F}_{10} \cdot x\text{H}_2\text{O}$  NPs of varying diameter (Figure 7(b)-(f)). All spectra are of fully hydrated samples unless otherwise stated, due to the much shorter  $^{19}\text{F}$   $T_1$  relaxation times arising from rapidly modulated  $^{19}\text{F}$ - $^1\text{H}$  dipolar couplings involving mobile  $\text{H}_2\text{O}$  molecules (*vide infra*), and correspondingly shorter experimental times. It is apparent that the spectra of the NPs, regardless of size, are clearly distinct from the bulk material in terms of the number of peaks, their relative intensities, and their isotropic chemical shifts. All NP samples have three distinct resonances ( $\delta_{\text{iso}} = -45$  to  $-51$  ppm, designated “**A**”,  $\delta_{\text{iso}} = -62$  ppm, “**B**”, and  $\delta_{\text{iso}} = -85$  ppm, “**C**”), none of which correspond to the shifts in the spectrum of bulk  $\text{YF}_3$ . The crystal structure of  $(\text{H}_3\text{O})\text{Y}_3\text{F}_{10} \cdot x\text{H}_2\text{O}$  (Table 2) has three unique fluorine sites *F1'*, *F2'*, and *F3'* (which we italicize and use prime symbols to differentiate from **F1** and **F2** in bulk  $\text{YF}_3$ ), with relative populations of 3:1:1, respectively (Figure 4). Integration in all of the  $^{19}\text{F}$  MAS NMR spectra of the NPs (Table 4) reveals a general ratio of 3:1:1 is apparent (including the intensities of both the



isotropic centerbands and the spinning sidebands), although this ratio varies somewhat with NP size (in particular, for the 21 and 132 nm NPs, see below for further discussion). From this ratio, Peak **A** should correspond to site  $F1'$ , and peaks **B** and **C** to  $F2'/F3'$ . The assignment of **B** and **C** is ambiguous because  $F2'$  and  $F3'$  reside in crystallographically similar sites and cannot be identified via  $^{19}\text{F}$  NMR without a priori knowledge of  $^{19}\text{F}$  chemical shift assignments. Unfortunately, due to the immense size of the  $(\text{H}_3\text{O})\text{Y}_3\text{F}_{10} \cdot x\text{H}_2\text{O}$  unit cell, first principles calculations using periodic boundary conditions were unable to aid in these chemical shift assignments.

**Table 4.** Relative integrated areas (including spinning sidebands) of resonances in  $^{19}\text{F}$  MAS NMR spectra of hydrated  $(\text{H}_3\text{O})\text{Y}_3\text{F}_{10} \cdot x\text{H}_2\text{O}$  nanoparticles and bulk  $\text{YF}_3$ . A, B, C, F1, and F2 refer to resonance labels, from high to low frequency (see Figure 7).

Size (nm)	Pulse delay (s)	Integrated Area (A:B:C)	Normalized Area (A:B:C) <sup>a</sup>
21	5	20.9 : 10.5 : 5.6	2.0 : 1.0 : 0.5
37	30	28.4 : 11.2 : 7.7	2.5 : 1.0 : 0.7
	5	31.2 : 11.4 : 7.9	2.8 : 1.0 : 0.7
49 (doped)	30	33.9 : 11.3 : 10.5	3.0 : 1.0 : 0.9
	5	39.4 : 11.9 : 10.4	3.3 : 1.0 : 0.9
67	30	35.8 : 11.0 : 9.2	3.2 : 1.0 : 0.8
	5	31.2 : 11.2 : 9.5	2.9 : 1.0 : 0.9
132	30	17.0 : 11.8 : 5.6	1.4 : 1.0 : 0.5
	5	18.4 : 11.3 : 6.0	1.6 : 1.0 : 0.5
		Integrated Area (F1:F2)	Normalized Ratio (F1:F2)
Bulk $\text{YF}_3$	5	4.9 : 10.0	1.0 : 2.0

<sup>a</sup> Numbers are normalized to the central resonance **B** and rounded to the first decimal place.

The assignment of resonances in  $^{19}\text{F}$  MAS spectra of the NPs was verified by considering their zeolithic properties. The 67 nm NP samples were dried in a lab oven at 125 °C and  $^{19}\text{F}$  NMR spectra were acquired immediately afterward. The effect of eliminating zeolithic water in the 67 nm  $(\text{H}_3\text{O})\text{Y}_3\text{F}_{10} \cdot x\text{H}_2\text{O}$  NP sample is shown in the  $^{19}\text{F}$  MAS NMR spectra in Figure 8. In  $^{19}\text{F}$  MAS NMR spectra of a fully hydrated sample (stored in air) of 67 nm  $(\text{H}_3\text{O})\text{Y}_3\text{F}_{10} \cdot x\text{H}_2\text{O}$  NPs (Figure 8(a),(b)), the expected 3:1:1 integration of  $FI':F2':F3'$  fluorine resonances is observed. However, when the sample was stored in a 125 °C oven prior to NMR experiments and packed in an airtight rotor (Figure 8(c)), the integration of  $FI':F2':F3'$  was found to be 1.7:1:1. This disparity in integrated intensities is believed to be due to the effects of proximate zeolithic  $\text{H}_2\text{O}$  on the  $T_1(^{19}\text{F})$  relaxation constants of the  $FI'$  sites, which form the channels and cavities of  $(\text{H}_3\text{O})\text{Y}_3\text{F}_{10} \cdot x\text{H}_2\text{O}$ . The  $\text{H}_2\text{O}$  molecules are wholly or partially mobile, which means that  $^1\text{H}$ - $^{19}\text{F}$  dipolar interactions continually fluctuate, contributing to efficient longitudinal  $^{19}\text{F}$  relaxation. This is evident from the nearly identical integrated areas resulting from experiments on hydrated samples using a long (30 s) and short (5 s) pulse delay (Table 4). However, when the presence of  $\text{H}_2\text{O}$  within  $(\text{H}_3\text{O})\text{Y}_3\text{F}_{10} \cdot x\text{H}_2\text{O}$  is reduced via heating, a drastic loss in integrated intensity of the  $FI'$  peak is observed in NMR experiments using the same 5 s pulse delay (*i.e.*,  $T_1(^{19}\text{F})$  relaxation is less efficient). No measurement/estimation of  $T_1(^{19}\text{F})$  associated with the  $FI'$  resonance within partially hydrated/heated  $(\text{H}_3\text{O})\text{Y}_3\text{F}_{10} \cdot x\text{H}_2\text{O}$  samples was attempted due to the very long recycle delays and experimental times required to acquire spectra with reasonable S/N (Figure S7). These findings are consistent with the assignment of peaks from the  $^{19}\text{F}$  MAS spectra. There is clearly efficient longitudinal relaxation associated with the  $F2'/F3'$  sites, owing to their environments within the ionic network of the UOA, and closer proximity to sources of fluctuating magnetic fields arising from mobile dipolar spin pairs.

The manifold of spinning sidebands that arises from a particular resonance in an MAS experiment (Figure 9) is important for the integration of individual resonances; but, these sidebands also encode information on the fluorine chemical shift (CS) tensors. Spinning sideband manifolds can be analyzed using the Herzfeld-Berger (HB) method to determine approximate CS tensor parameters,<sup>92</sup> though at high spinning rates, the low number of high intensity spinning sidebands limits this analysis. Of the three  $^{19}\text{F}$  resonances associated with  $(\text{H}_3\text{O})\text{Y}_3\text{F}_{10} \cdot x\text{H}_2\text{O}$ , **A** has the highest chemical shift anisotropy (CSA) (*i.e.*, highest span ( $\Omega$ ) value, Table 5). In contrast, **B** and **C** have smaller  $\Omega$  values ranging from 110 to 120 ppm and 90 to 130 ppm, respectively. The values of  $\delta_{\text{iso}}$  and  $\Omega$  associated with **B** and **C** resemble those originating from sites **F1** and **F2** in bulk  $\text{YF}_3$ . Skew ( $\kappa$ ) values for **B** range from 0.1 to 0.5, which correspond well with the  $\kappa$  value of 0.3 associated with site **F2** in bulk  $\text{YF}_3$ . However, the absence of spinning sidebands (due to a small CSA) associated with both resonance **C** in the NP samples and **F1** in the bulk sample makes it difficult to compare their  $\kappa$  values. The similarity of the isotropic chemical shifts and spans of resonances **B** and **C** ( $F2'/F3'$ ) in  $(\text{H}_3\text{O})\text{Y}_3\text{F}_{10} \cdot x\text{H}_2\text{O}$  NPs to those of **F2** and **F1** in bulk  $\text{YF}_3$  suggest that their chemical environments may also be similar.

The **A** resonances have numerous spinning sidebands, which are analyzed to yield CS tensor parameters ( $\Omega = 180$  to  $200$  ppm,  $\kappa = 0.6$  to  $0.9$ ) which are unique from those of **B**, **C**, **F1**, and **F2**. This strongly indicates that the structural environment of the **A** fluorines within the  $(\text{H}_3\text{O})\text{Y}_3\text{F}_{10} \cdot x\text{H}_2\text{O}$  NPs is distinct from the known environments of the bulk  $\text{YF}_3$  phase. It has been suggested that H-O-H...F hydrogen bonding is present in systems similar to  $(\text{H}_3\text{O})\text{Y}_3\text{F}_{10} \cdot x\text{H}_2\text{O}$ .<sup>77</sup>  $FI'$ -O distances in our refined crystal structure are  $2.5 \text{ \AA}$ , within the hydrogen bonding range in metal fluoride hydrates,<sup>93</sup> which may partially account for the unique CS tensor parameters associated with

A. A correlation also exists between the  $\delta_{\text{iso}}$  (**A**) and  $(\text{H}_3\text{O})\text{Y}_3\text{F}_{10} \cdot x\text{H}_2\text{O}$  NP size: as the NP size decreases, the chemical shift varies from -51 ppm to -45 ppm (Figure 10). It is notable that  $\delta_{\text{iso}}$  (**A**) does not change with hydration level of the NPs (*vide supra*).

**Table 5.**  $^{19}\text{F}$  chemical shift tensor parameters extracted from MAS spectra of hydrated  $(\text{H}_3\text{O})\text{Y}_3\text{F}_{10} \cdot x\text{H}_2\text{O}$  nanoparticles and bulk  $\text{YF}_3$  via Herzfeld-Berger analysis of spinning sidebands.

NP Size (nm)	Peak Label <sup>a</sup>	Individual CS Tensor Components <sup>c</sup>					$\kappa$ <sup>e</sup>
		$\delta_{\text{iso}}$ (ppm) <sup>b</sup>	$\delta_{11}$ (ppm)	$\delta_{22}$ (ppm)	$\delta_{33}$ (ppm)	$\Omega$ (ppm) <sup>d</sup>	
21	A	-51(2)	19(15)	-8(19)	-161(21)	180(30)	0.7(3)
	B	-62(2)	-10(19)	-46(17)	-130(24)	120(40)	0.4(4)
	C	-85(2)	-41(17)	-53(19)	-161(27)	120(40)	0.8(4)
37	A	-49(2)	31(16)	-9(21)	-169(21)	200(30)	0.6(3)
	B	-62(2)	-9(21)	-58(15)	-118(22)	110(40)	0.1(4)
	C	-86(2)	-56(18)	-56(28)	-146(29)	90(40)	1.0(8) <sup>f</sup>
49	A	-49(2)	14(19)	5(27)	-166(29)	180(40)	0.9(4)
	B	-61(2)	-11(19)	41(17)	-131(25)	120(40)	0.5(4)
	C	-85(2)	-31(19)	-63(19)	-160(25)	130(40)	0.5(4)
67	A	-47(2)	26(15)	6(22)	-173(22)	200(30)	0.8(3)
	B	-62(2)	-10(19)	-46(17)	-130(24)	120(40)	0.4(4)
	C	-85(2)	-25(29)	-115(25)	-115(17)	90(40)	-1.0(7) <sup>f</sup>
132	A	-45(2)	28(18)	0(20)	-162(27)	190(40)	0.7(3)
	B	-61(2)	-3(21)	-57(16)	-123(22)	120(40)	0.1(4)
	C	-84(2)	-38(18)	-66(16)	-148(25)	110(40)	0.5(4)
Bulk	F2	-56(2)	-2(15)	-44(13)	-122(18)	120(30)	0.3(3)
	F1	-67(2)	20(31)	-110(33)	-110(20)	130(40)	-1.0(7) <sup>f</sup>

<sup>a</sup> See Figure 7 for labelled spectra. <sup>b</sup> Isotropic chemical shift:  $\delta_{\text{iso}} = (\delta_{11} + \delta_{22} + \delta_{33})/3$ .

<sup>c</sup> Individual CS tensor components and associated uncertainties calculated from experimentally measured  $\delta_{\text{iso}}$ ,  $\Omega$ , and  $\kappa$  values. <sup>d</sup> Span:  $\Omega = \delta_{11} - \delta_{33}$ . <sup>e</sup> Skew:  $\kappa = 3(\delta_{22} - \delta_{\text{iso}})/\Omega$ . <sup>f</sup>  $\kappa$  value associated with a high uncertainty due to lack of spinning sidebands.

The crystal structure of  $(\text{H}_3\text{O})\text{Y}_3\text{F}_{10} \cdot x\text{H}_2\text{O}$  (Table 2) has three unique fluorine sites in a ratio of 3:1:1, this ratio correlates well with the ratios of the integrated intensities from the  $^{19}\text{F}$  MAS NMR spectra of the 37, 49, and 67 nm NPs (Table 4). The synthesis of the  $(\text{H}_3\text{O})\text{Y}_3\text{F}_{10} \cdot x\text{H}_2\text{O}$  NPs is closely related to the synthesis of amorphous  $\text{YF}_3$  NPs;<sup>20</sup> it follows that any presence of this amorphous  $\text{YF}_3$  phase as an impurity within the NP samples will affect the  $^{19}\text{F}$  NMR spectrum. Specifically, since the amorphous  $\text{YF}_3$  phase exhibits a similar chemical shift to **B**, the presence of  $\text{YF}_3$  may influence the integrated intensity of the **B** resonance in  $(\text{H}_3\text{O})\text{Y}_3\text{F}_{10} \cdot x\text{H}_2\text{O}$  NP spectra, as both  $^{19}\text{F}$  NMR resonances arising from crystalline bulk  $\text{YF}_3$  (**F1** and **F2**) are proximate to this resonance. Indeed, the integration ratios of the  $^{19}\text{F}$  MAS NMR spectra for the 21 nm NPs (2.0 : 1.0 : 0.5) and 132 nm NPs (1.6 : 1.0 : 0.5) are distinct from the predicted 3 : 1 : 1 ratio due to broad patterns underlying the **B** resonance, hinting at the presence of  $\text{YF}_3$  in these samples. It is notable that this apparent  $\text{YF}_3$  impurity is detectable via SSNMR experiments but not pXRD experiments, indicating that this impurity is amorphous. In order to further investigate the structure of the NPs and the nature of the impurity,  $^{19}\text{F}$ - $^{89}\text{Y}$  VACP/MAS experiments were performed.

**$^{19}\text{F}$ - $^{89}\text{Y}$  VACP/MAS NMR experiments.**  $^{89}\text{Y}$  is a low- $\gamma$  nucleus, and in most inorganic compounds is associated with large  $T_1(^{89}\text{Y})$  values (*i.e.*, inefficient longitudinal relaxation), which can lead to long experimental times.<sup>64</sup> Accordingly,  $^{19}\text{F}$ - $^{89}\text{Y}$  VACP/MAS experiments were employed to exploit the potentially large polarization transfer from  $^{19}\text{F}$  to  $^{89}\text{Y}$ , as well as the shorter  $T_1(^{19}\text{F})$ .<sup>72,94</sup> The  $^{19}\text{F}$ - $^{89}\text{Y}$  VACP/MAS spectrum of bulk  $\text{YF}_3$  is shown in Figure 11(a). As expected from the crystal structure (Figure 6), there is a sole resonance corresponding to a single crystallographically unique nine-coordinate yttrium site.

The  $^{19}\text{F}$ - $^{89}\text{Y}$  VACP/MAS spectra of hydrated  $(\text{H}_3\text{O})\text{Y}_3\text{F}_{10} \cdot x\text{H}_2\text{O}$  NPs (Figure 11) are clearly distinct from the bulk material. The crystal structure of  $(\text{H}_3\text{O})\text{Y}_3\text{F}_{10} \cdot x\text{H}_2\text{O}$  indicates a single Y site and therefore a sole  $^{89}\text{Y}$  resonance, but there are two  $^{89}\text{Y}$  resonances visible in the NP spectra: one of high intensity at ca.  $\delta_{\text{iso}} = -55$  ppm (denoted “**X**” for discussion, Figure 11) and a resonance of low, but also NP size-dependent, intensity at  $\delta_{\text{iso}} = -36$  ppm (denoted “**W**”). The integrated area of **W** is strongly linked to NP size: as the NP size decreases, the relative area of **W** in comparison to **X** increases (Table 6, Figure 12). The relationship between NP size and  $^{89}\text{Y}$  NMR integrated area ratio follows a similar exponential trend as the ratio of octahedron surface area to volume, leading to the preliminary interpretation that **W** may correspond to a Y position on or near the NP surface, while **X** may be associated with a Y position deeper in the NP core. The only exception are the 49 nm Sc-doped NPs, where the 5 mol % Sc doping seems to affect the overall structure enough that  $^{89}\text{Y}$  chemical shifts are distinct from the other samples.

**Table 6.** Relative integrated areas (including spinning sidebands) of resonances in  $^{19}\text{F}$ - $^{89}\text{Y}$  VACP/MAS NMR spectra of hydrated  $(\text{H}_3\text{O})\text{Y}_3\text{F}_{10} \cdot x\text{H}_2\text{O}$  nanoparticles. <sup>a</sup> See Figures 11, 12.

Nanoparticle Size (nm)	$\delta_{\text{iso}}$ (ppm)	Relative Integrated Area	Peak Integration Ratio <sup>b</sup>	
			<i>Experimental</i>	<i>Octahedron</i> <sup>c</sup>
21	-36(2)	4.37(24)	0.437	0.35
	-54(2)	10		
37	-38(2)	2.62(16)	0.262	0.199
	-55(2)	10		
67	-36(2)	1.29(9)	0.129	0.11
	-58(2)	10		
132	-36(2)	0.78(18)	0.078	0.06
	-56(2)	10		
49 <sup>d</sup>	-36(2)	3.37(28)	0.337	0.15
	-56(2)	10		
83 <sup>e</sup>	-23(3)	0.65(15)	0.065	0.089
	-54(3)	10		

<sup>a</sup> Bulk  $\text{YF}_3$  only has one  $^{89}\text{Y}$  resonance, thus integration not applicable to this sample. <sup>b</sup> Refers to the ratio of the area of the “surface-like”  $^{89}\text{Y}$  resonance at ca. -36 ppm versus that of “core-like”  $^{89}\text{Y}$  at ca. -55 ppm. <sup>c</sup> Refers to the ratio of surface area to total volume of an ideal octahedron of specified NP edge length, using the formulae  $A = 2(\sqrt{3})x^2$  and  $V = 1/3(\sqrt{2})x^3$ . <sup>d</sup> Since this sample has a major structural change (the presence of Sc, likely in Y sites), its peak integration ratio results in an outlying value. <sup>e</sup> The 83 nm samples were synthesized at a separate point in time, using a similar procedure as for all other NPs. See Experimental section.

Neither of the two major resonances in the spectra of the  $(\text{H}_3\text{O})\text{Y}_3\text{F}_{10} \cdot x\text{H}_2\text{O}$  NPs correspond to bulk  $\text{YF}_3$ ; however, there is a broad, low-intensity peak at ca.  $\delta_{\text{iso}} = -105$  to  $-110$  ppm, which is most prominent in the spectra of the 21 and 132 nm  $(\text{H}_3\text{O})\text{Y}_3\text{F}_{10} \cdot x\text{H}_2\text{O}$  NP samples, less intense in the spectrum of the 49 nm NPs, and barely visible in the spectra of the 37 and 67 nm samples, consistent with earlier conclusions regarding the presence of an amorphous  $\text{YF}_3$  impurity as



suggested by variation in the integrated intensities of  $^{19}\text{F}$  MAS NMR resonances. TEM experiments indicate that all samples are composed primarily of monodisperse crystalline NPs, with trace populations of spherical amorphous NPs (see Experimental section),<sup>20</sup> and SSNMR reveals a broad resonance corresponding to bulk  $\text{YF}_3$  impurity for some of the samples; hence, the spherical amorphous NPs are likely composed of amorphous  $\text{YF}_3$ . A less likely possibility also exists that a small fraction of the crystalline NPs may be fully or partially composed of crystalline bulk  $\text{YF}_3$ , although evidence of this was not observed in our experiments. Further, from the synthetic procedure and parameters given in the Experimental section (*vide supra*), it appears as if the use of AOT surfactant in NP synthesis suppresses the formation of  $\text{YF}_3$ . Differences in experimental  $^{19}\text{F}$ - $^{89}\text{Y}$  CP mixing times did not have an effect on the integration or intensities of the individual peaks associated with  $(\text{H}_3\text{O})\text{Y}_3\text{F}_{10} \cdot x\text{H}_2\text{O}$  (Figure S8).

A separate batch of 83 nm  $(\text{H}_3\text{O})\text{Y}_3\text{F}_{10} \cdot x\text{H}_2\text{O}$  NPs, synthesized in a similar manner (but at a later date), were employed to study the effects of sample hydration on  $^{19}\text{F}$ - $^{89}\text{Y}$  VACP(/MAS) NMR spectra and to confirm the assignments of the **W** and **X** resonances (see Experimental); these NPs have similar TEM images (Figure S9) and NMR spectra (*vide infra*) to those of the initial batches of  $(\text{H}_3\text{O})\text{Y}_3\text{F}_{10} \cdot x\text{H}_2\text{O}$  NPs. Both resonances **W** and **X** are present in  $^{19}\text{F}$ - $^{89}\text{Y}$  VACP/MAS NMR spectra of the partially and fully hydrated 83 nm NP samples (Figure 13), although the resolution of the **W** peak in the spectrum of the former is very poor, translating to sizable uncertainty regarding its exact position and breadth (Table 6, Table S5). The spectrum of the fully hydrated 83 nm NP sample displays higher S/N and much better resolution of the **W** and **X** sites, although both spectra were recorded with similar acquisition parameters. Y sites in the partially dehydrated sample may be strongly, weakly, or not coordinated to surface  $\text{H}_2\text{O}$  species; hence, the broad and poorly resolved

**W** peaks in these samples likely arises from (i) a distribution of  $^{89}\text{Y}$  chemical shifts and/or (ii) a distribution of  $T_2(^{89}\text{Y})$  constants, originating from interactions between surface yttria and water molecules. The hydration-linked changes in these  $^{19}\text{F}$ - $^{89}\text{Y}$  VACP/MAS NMR spectra confirm that resonance **W** corresponds to a Y position on or near the NP surface, while **X** is linked with a Y position within the NP core

**Static  $^{19}\text{F}$ - $^{89}\text{Y}$  VACP NMR experiments.** The sensitivity of  $^{19}\text{F}$ - $^{89}\text{Y}$  VACP/MAS NMR spectra to surface- and core-like yttrium environments invites examination of the complete  $^{89}\text{Y}$  CS tensor parameters. In order to extract anisotropic  $^{89}\text{Y}$  CS tensor parameters, static (non-spinning) VACP experiments were performed. The NMR spectra obtained for the NP samples of all sizes are distinct from bulk  $\text{YF}_3$  (Figure 14), which exhibits a distinct powder pattern from which CS tensor parameters are readily extracted. All of the hydrated  $(\text{H}_3\text{O})\text{Y}_3\text{F}_{10} \cdot x\text{H}_2\text{O}$  NP samples have spectra which suggest the presence of multiple sites and perhaps some degree of disorder. An impurity, identified as bulk  $\text{YF}_3$ , makes small contributions to all powder patterns in the region of  $\delta_{\text{iso}} = -107$  ppm (*vide supra*).

It is possible to simulate the static  $^{19}\text{F}$ - $^{89}\text{Y}$  VACP powder patterns of the bulk sample and the NPs and extract their respective  $^{89}\text{Y}$  CS tensor parameters (Table 7, Figure 15). Bulk  $\text{YF}_3$  (Figure 15(a)) yields a well-defined powder pattern which corresponds to CS tensor parameters of  $\Omega = 110(5)$  ppm and  $\kappa = 0.20(5)$ . Simulations of NP spectra feature two  $^{89}\text{Y}$  resonances, with relative integrated intensities and  $\delta_{\text{iso}}$  closely resembling those obtained from the corresponding VACP/MAS experiments. Owing to the lack of distinct features in all of the NP powder patterns, the  $^{89}\text{Y}$  CS tensor parameters have a higher degree of uncertainty than those of the bulk sample. The

two  $^{89}\text{Y}$  powder patterns evident in spectra of  $(\text{H}_3\text{O})\text{Y}_3\text{F}_{10} \cdot x\text{H}_2\text{O}$  NPs of all sizes correspond to CS tensor parameters of  $\Omega = 50(10)$  ppm and  $\kappa = -0.4(1)$ .

**Table 7.**  $^{89}\text{Y}$  CS tensor parameters extracted from static  $^{19}\text{F}$ - $^{89}\text{Y}$  VACP NMR experiments on hydrated  $(\text{H}_3\text{O})\text{Y}_3\text{F}_{10} \cdot x\text{H}_2\text{O}$  NPs. <sup>a</sup>

Nanoparticle Size (nm)	$\delta_{\text{iso}}$ (ppm)	$\Omega$ (ppm)	$\kappa$	Relative Intensity (%)
21	-36(3)	50(10)	-0.4(1)	42
	-54(3)	50(10)	-0.4(1)	100
37	-38(3)	50(10)	-0.4(1)	26
	-55(3)	50(10)	-0.4(1)	100
49	-36(3)	50(10)	-0.4(1)	35
	-54(4) <sup>b</sup>	50(10)	-0.4(1)	100
67	-36(3)	50(10)	-0.4(1)	13
	-55(4) <sup>b</sup>	50(10)	-0.4(1)	100
132	-36(3)	50(10)	-0.4(1)	20 <sup>c</sup>
	-54(4) <sup>b</sup>	50(10)	-0.4(1)	100
Bulk $\text{YF}_3$	-107(2)	110(5)	0.20(5)	-
83 <sup>d</sup>	-28(3)	50 (10)	-0.4(1)	19
(Fully hydrated)	-55(3) <sup>b</sup>	50 (10)	-0.4(1)	100
83 <sup>d,e</sup>	-28(5)	60(20)	-0.4(2)	18
(Partially hydrated)	-54(4) <sup>b</sup>	60(20)	-0.4(2)	100

<sup>a</sup> All simulations of spectra required ca. 175 Hz of line broadening. <sup>b</sup>  $\delta_{\text{iso}}$  of static simulation differs from VACP/MAS result. <sup>c</sup> Relative intensity of static simulation differs from that of VACP/MAS experiment. <sup>d</sup> Refers to a NP sample prepared separately but in a similar manner, see discussion in text. <sup>e</sup> The fully hydrated sample yields a relatively broad, featureless lineshape, which provides little data about the CS tensor. This is reflected in the associated uncertainty of parameters for this sample.

Static  $^{19}\text{F}$ - $^{89}\text{Y}$  VACP experiments were also performed on partially and fully hydrated 83 nm  $(\text{H}_3\text{O})\text{Y}_3\text{F}_{10} \cdot x\text{H}_2\text{O}$  NPs (Figure 16, Table 7). The most striking differences between these spectra are the breadths and shapes of the powder patterns. Much like the VACP/MAS spectra, the spectrum of the partially hydrated NPs is broader and the individual patterns are more difficult to resolve in comparison to those of the fully hydrated NPs; this is consistent with the notion that there are larger distributions of chemical shifts and/or  $T_2(^{89}\text{Y})$  values associated with the “W” powder pattern centered at  $\delta_{\text{iso}} = -36$  ppm. Fully and partially hydrated samples give rise to two sets of similar  $^{89}\text{Y}$  CS parameters which are differentiated by  $\delta_{\text{iso}}$  (Table 7), but share common anisotropic parameters (*i.e.*,  $\Omega$  and  $\kappa$ ).

## Conclusions

We have shown, using powder XRD and SSNMR methods, that the intended reverse micelle synthesis of  $\text{YF}_3$  NPs yields crystalline NPs of controllable size and shape, with a distinct composition and phase  $(\text{H}_3\text{O})\text{Y}_3\text{F}_{10} \cdot x\text{H}_2\text{O}$ . The zeolitic channels and cavities are populated by hydrogen-bound water molecules. Residual surfactant from the synthesis is limited to the NP surface in relatively small amounts.  $^{19}\text{F}$  MAS NMR spectra show a clear difference in phase between bulk  $\text{YF}_3$  and the NP samples: three unique resonances are observed for the latter, in accordance with the crystal structure of  $(\text{H}_3\text{O})\text{Y}_3\text{F}_{10} \cdot x\text{H}_2\text{O}$ . The integration of these resonances, along with extracted  $^{19}\text{F}$  CS tensor parameters, allow for their partial assignment. The  $^{19}\text{F}$  nuclei corresponding to the fluorine resonance A, which are demonstrated to compose the zeolitic channels and cavities, have longer  $T_1$  relaxation times when  $\text{H}_2\text{O}$  is not present within the sample, owing to the reduction of rapidly modulated  $^{19}\text{F}$ - $^1\text{H}$  dipolar couplings that serve to increase the efficiency of longitudinal

relaxation.  $^{19}\text{F}$ - $^{89}\text{Y}$  VACP/MAS spectra of  $(\text{H}_3\text{O})\text{Y}_3\text{F}_{10} \cdot x\text{H}_2\text{O}$  NPs exhibit two resonances of dissimilar intensity which do not correspond to bulk  $\text{YF}_3$ ; the less intense resonance has an integrated area directly correlated to NP size and is linked to surface-like yttrium environments. MAS and static  $^{19}\text{F}$ - $^{89}\text{Y}$  spectra of partially hydrated samples confirm that two  $^{89}\text{Y}$  resonances are present. The less intense  $^{89}\text{Y}$  resonance associated with surface yttrium species is especially difficult to resolve in the partially hydrated species, since surface Y sites may or may not be interacting with water molecules, leading to a distribution of  $^{89}\text{Y}$  chemical shifts and/or  $T_2(^{89}\text{Y})$  constants. Static  $^{19}\text{F}$ - $^{89}\text{Y}$  VACP experiments show that the surface and core yttrium environments associated with these  $(\text{H}_3\text{O})\text{Y}_3\text{F}_{10} \cdot x\text{H}_2\text{O}$  NPs are similar, confirming only small amounts of ligands and surfactant are bound to the NP surface. Finally, with knowledge of the intended product and synthetic precursors, along with the combined use of pXRD and SSNMR, we have demonstrated that it is possible to identify an NP product, probe its macroscopic zeolithic behaviour at the molecular level, link NMR resonances to overall NP size, establish product purity with respect to contaminants, and determine the identity and morphology of the impurities. This experimental protocol offers much promise for the identification, characterization, and future rational design of NPs.

## Acknowledgements

BEGL thanks the Ontario Ministry of Training, Colleges, and Universities for a Queen Elizabeth II Ontario Graduate Scholarship in Science and Technology (QEII-GSST). RWS thanks the Natural Sciences and Engineering Research Council (NSERC, Canada), the Canadian Foundation for Innovation, the Ontario Innovation Trust and the University of Windsor for support. RWS also thanks the Ontario Ministry of Research and Innovation for an Early Researcher Award, and

acknowledges the Centre for Catalysis and Materials Research (CCMR) at the University of Windsor for additional funding. JLL, AB, MB, and AMR would like to acknowledge NanoQuébec, le Fonds Québécois de la recherche sur la nature et les technologies (FQRNT) and NSERC for their financial support.

**Supporting Information Available:** Additional information on Rietveld refinements of pXRD data, complete NMR experimental parameters, additional  $^1\text{H}$  and  $^{19}\text{F}$ - $^{89}\text{Y}$  NMR spectrum integrations, supplemental  $^1\text{H}$ ,  $^{19}\text{F}$ ,  $^{19}\text{F}$ - $^{89}\text{Y}$ , and  $^1\text{H}$ - $^{13}\text{C}$  NMR spectra, and TEM images of 83 nm nanoparticles. This material is available free of charge *via* the Internet at <http://pubs.acs.org>.

### Figure Captions

**Figure 1.** TEM images of octahedrally-shaped  $(\text{H}_3\text{O})\text{Y}_3\text{F}_{10} \cdot x\text{H}_2\text{O}$  nanoparticles, with a measured edge length of (a) 21 nm, (b) 37 nm, (c) 49 nm, (d) 67 nm, and (e) 132 nm. Octahedron edges shown in (d) are highlighted to demonstrate NP measurements.

**Figure 2.** pXRD patterns collected for bulk  $\text{YF}_3$  (space group  $Pnma$ ) and  $(\text{H}_3\text{O})\text{Y}_3\text{F}_{10} \cdot x\text{H}_2\text{O}$  nanoparticles, (space group  $Fd-3m$ ), with nanoparticle diameters listed in nm. A simulated pXRD pattern for bulk  $\text{YF}_3$  is displayed at the bottom.

**Figure 3.** Rietveld profile for the 67 nm diameter  $(\text{H}_3\text{O})\text{Y}_3\text{F}_{10} \cdot x\text{H}_2\text{O}$  nanoparticles using the space group  $Fd-3m$ .

**Figure 4.** Schematic representation of the  $(\text{H}_3\text{O})\text{Y}_3\text{F}_{10} \cdot x\text{H}_2\text{O}$  diamond-like structure where (a) represents the  $\text{YF}_8$  coordination polyhedra, (b) represents the  $[\text{Y}_6\text{F}_{32}]^{14-}$  UOA octahedral-like building units, (c) and (d) represent the cage like structure exhibited by the nanoparticles. Fluorine ions are denoted by blue spheres and the yttrium polyhedra are denoted in grey. In (c) the red spheres denote the oxygen ions associated with the  $\text{H}_3\text{O}^+$  moiety and in (d) the purple spheres indicate the void spaces. The positions of the water molecules within the cages are not shown.

**Figure 5.**  $^1\text{H}$  MAS spectra of 67 nm  $(\text{H}_3\text{O})\text{Y}_3\text{F}_{10} \cdot x\text{H}_2\text{O}$  nanoparticles at a spinning speed of 25 kHz. The red trace corresponds to a fully hydrated ( $x = 1$ ) sample, and the blue trace corresponds to a partially hydrated ( $x < 1$ ) sample. Inset left:  $(\text{H}_3\text{O})\text{Y}_3\text{F}_{10} \cdot x\text{H}_2\text{O}$  crystal structure.

**Figure 6.** (a) The local nine-coordinate environment about yttrium and (b) the extended structure of bulk  $\text{YF}_3$ . There are two fluorine sites in a 1:2 ratio and one unique yttrium center.

**Figure 7.**  $^{19}\text{F}$  MAS NMR spectra of (a) bulk  $\text{YF}_3$  and hydrated  $(\text{H}_3\text{O})\text{Y}_3\text{F}_{10} \cdot x\text{H}_2\text{O}$  nanoparticles of size (b) 132 nm, (c) 67 nm, (d) 49 nm, (e) 37 nm, and (f) 21 nm. Spectra recorded at a spinning speed of 25 kHz. F1 and F2 in (a) denote isotropic chemical shifts in bulk  $\text{YF}_3$ , A, B, and C for (b)-(f) denote isotropic chemical shifts in  $(\text{H}_3\text{O})\text{Y}_3\text{F}_{10} \cdot x\text{H}_2\text{O}$ , while asterisks (\*) denote spinning sidebands.

**Figure 8.**  $^{19}\text{F}$  MAS NMR spectra for 67 nm  $(\text{H}_3\text{O})\text{Y}_3\text{F}_{10} \cdot x\text{H}_2\text{O}$  nanoparticles (a) as received (hydrated), (b) after prolonged air exposure (hydrated), (c) after 12 hours of heating at 125 °C

(partially hydrated). Spectra were recorded at a spinning speed of 25 kHz. Peak labels indicate resonance assignment and integration ratios (including spinning sidebands). Asterisks (\*) denote spinning sidebands.

**Figure 9.** Deconvoluted  $^{19}\text{F}$  MAS NMR spectra of hydrated 37 nm  $(\text{H}_3\text{O})\text{Y}_3\text{F}_{10} \cdot x\text{H}_2\text{O}$  nanoparticles. Spinning sidebands are labeled according to the corresponding isotropic peak. Spectra were recorded at a spinning speed of 25 kHz.

**Figure 10.** Change in  $\delta_{\text{iso}}$  of resonance A correlated with nanoparticle size in  $^{19}\text{F}$  MAS NMR spectra of hydrated  $(\text{H}_3\text{O})\text{Y}_3\text{F}_{10} \cdot x\text{H}_2\text{O}$  nanoparticles of size (b) 132 nm, (c) 67 nm, (d) 49 nm, (e) 37 nm, and (f) 21 nm. Bulk  $\text{YF}_3$  is shown in (a) for comparison. Spectra recorded at a spinning speed of 25 kHz. A, B, and C denote isotropic chemical shifts in hydrated  $(\text{H}_3\text{O})\text{Y}_3\text{F}_{10} \cdot x\text{H}_2\text{O}$ .

**Figure 11.**  $^{19}\text{F}$ - $^{89}\text{Y}$  VACP/MAS NMR spectra of bulk  $\text{YF}_3$  (a) and hydrated  $(\text{H}_3\text{O})\text{Y}_3\text{F}_{10} \cdot x\text{H}_2\text{O}$  nanoparticles of size (b) 132 nm, (c) 67 nm, (d) 49 nm, (e) 37 nm, and (f) 21 nm. Spectra recorded at a spinning speed of 5 kHz. Inset left: The dashed grey line indicates traces of bulk  $\text{YF}_3$  exist as various degrees of impurity in the  $(\text{H}_3\text{O})\text{Y}_3\text{F}_{10} \cdot x\text{H}_2\text{O}$  nanoparticle samples.

**Figure 12.** The graph depicts the relationship between the ratio of the integrated areas of **W** and **X** peaks and  $(\text{H}_3\text{O})\text{Y}_3\text{F}_{10} \cdot x\text{H}_2\text{O}$  NP size in  $^{19}\text{F}$ - $^{89}\text{Y}$  VACP/MAS spectra of hydrated samples. Blue data points represent experimental ratios, red data points represent surface area/volume ratios of ideal



octahedra (see Table 6). The green outlier represents the 49 nm Sc-doped  $(\text{H}_3\text{O})\text{Y}_3\text{F}_{10} \cdot x\text{H}_2\text{O}$  nanoparticles.

**Figure 13.**  $^{19}\text{F}$ - $^{89}\text{Y}$  VACP/MAS NMR spectra of 83 nm  $(\text{H}_3\text{O})\text{Y}_3\text{F}_{10} \cdot x\text{H}_2\text{O}$  nanoparticles, where (a) is a fully hydrated sample, and (b) is only partially hydrated. Spectra were recorded at a spinning speed of 5 kHz.

**Figure 14.** Static  $^{19}\text{F}$ - $^{89}\text{Y}$  VACP NMR spectra of (a) bulk  $\text{YF}_3$  and hydrated  $(\text{H}_3\text{O})\text{Y}_3\text{F}_{10} \cdot x\text{H}_2\text{O}$  nanoparticles of size (b) 132 nm, (c) 67 nm, (d) 49 nm, (e) 37 nm, and (f) 21 nm.

**Figure 15.** Static  $^{19}\text{F}$ - $^{89}\text{Y}$  VACP NMR spectra and simulation of (a) bulk  $\text{YF}_3$  and (b) hydrated 37 nm  $(\text{H}_3\text{O})\text{Y}_3\text{F}_{10} \cdot x\text{H}_2\text{O}$  nanoparticles. See Table 7.

**Figure 16.** Overlaid static  $^{19}\text{F}$ - $^{89}\text{Y}$  VACP NMR spectra of fully (black) and partially (orange) hydrated 83 nm  $(\text{H}_3\text{O})\text{Y}_3\text{F}_{10} \cdot x\text{H}_2\text{O}$  nanoparticles are shown in (a). Simulations of spectra of the fully ((b), inset left), and partially ((c), inset right) hydrated NPs are also shown. See Table 7.

## References

- (1) Anker, J. N.; Hall, W. P.; Lyandres, O.; Shah, N. C.; Zhao, J.; Van Duyne, R. P. *Nat. Mater.* **2008**, *7*, 442.
- (2) Brigger, I.; Dubernet, C.; Couvreur, P. *Adv. Drug Delivery Rev.* **2002**, *54*, 631.
- (3) Hutter, E.; Fendler, J. H. *Adv. Mater.* **2004**, *16*, 1685.
- (4) Klimov, V. I.; Mikhailovsky, A. A.; Xu, S.; Malko, A.; Hollingsworth, J. A.; Leatherdale, C. A.; Eisler, H. J.; Bawendi, M. G. *Science* **2000**, *290*, 314.
- (5) Lal, S.; Link, S.; Halas, N. J. *Nat. Photonics* **2007**, *1*, 641.
- (6) Panyam, J.; Labhasetwar, V. *Adv. Drug Delivery Rev.* **2003**, *55*, 329.
- (7) Wang, X.; Zhuang, J.; Peng, Q.; Li, Y. D. *Nature* **2005**, *437*, 121.
- (8) Wang, X.; Li, Y. D. *Chem. Eur. J.* **2003**, *9*, 5627.
- (9) Mai, H. X.; Zhang, Y. W.; Si, R.; Yan, Z. G.; Sun, L. D.; You, L. P.; Yan, C. H. *J. Am. Chem. Soc.* **2006**, *128*, 6426.
- (10) Chan, W. C. W.; Maxwell, D. J.; Gao, X. H.; Bailey, R. E.; Han, M. Y.; Nie, S. M. *Curr. Opin. Biotechnol.* **2002**, *13*, 40.
- (11) Bunzli, J. C. G. *Acc. Chem. Res.* **2006**, *39*, 53.
- (12) Chatterjee, D. K.; Rufalhah, A. J.; Zhang, Y. *Biomaterials* **2008**, *29*, 937.
- (13) Boyer, J. C.; Cuccia, L. A.; Capobianco, J. A. *Nano Lett.* **2007**, *7*, 847.
- (14) Heer, S.; Lehmann, O.; Haase, M.; Gudel, H. U. *Angew. Chem. Int. Ed.* **2003**, *42*, 3179.
- (15) Wang, F.; Han, Y.; Lim, C. S.; Lu, Y. H.; Wang, J.; Xu, J.; Chen, H. Y.; Zhang, C.; Hong, M. H.; Liu, X. G. *Nature* **2010**, *463*, 1061.
- (16) Wang, F.; Liu, X. G. *J. Am. Chem. Soc.* **2008**, *130*, 5642.

- (17) Wang, F.; Liu, X. G. *Chem. Soc. Rev.* **2009**, 38, 976.
- (18) Tissue, B. M. *Chem. Mat.* **1998**, 10, 2837.
- (19) Stouwdam, J. W.; Hebbink, G. A.; Huskens, J.; van Veggel, F. C. J. M. *Chem. Mat.* **2003**, 15, 4604.
- (20) Lemyre, J. L.; Ritcey, A. M. *Chem. Mat.* **2005**, 17, 3040.
- (21) Lemyre, J. L.; Lamarre, S.; Beaupre, A.; Ritcey, A. M. *Langmuir* **2011**, 27, 11824.
- (22) Fedorov, P. P.; Luginina, A. A.; Kuznetsov, S. V.; Osiko, V. V. *J. Fluorine Chem.* **2011**, 132, 1012.
- (23) Li, C. X.; Lin, J. J. *J. Mat. Chem.* **2010**, 20, 6831.
- (24) Vetrone, F.; Capobianco, J. A. *Int. J. Nanotechnol.* **2008**, 5, 1306.
- (25) Kuznetsov, S. V.; Osiko, V. V.; Tkatchenko, E. A.; Fedorov, P. P. *Russ. Chem. Rev.* **2006**, 75, 1065.
- (26) Yi, G. S.; Lu, H. C.; Zhao, S. Y.; Yue, G.; Yang, W. J.; Chen, D. P.; Guo, L. H. *Nano Lett.* **2004**, 4, 2191.
- (27) Lu, H. C.; Yi, G. S.; Zhao, S. Y.; Chen, D. P.; Guo, L. H.; Cheng, J. J. *J. Mat. Chem.* **2004**, 14, 1336.
- (28) Guo, H. C.; Qian, H. S.; Idris, N. M.; Zhang, Y. *Nanomed. Nanotechnol. Biol. Med.* **2010**, 6, 486.
- (29) Rossetti, F. C.; Fantini, M. C. A.; Carollo, A. R. H.; Tedesco, A. C.; Bentley, M. J. *J. Pharm. Sci.* **2011**, 100, 2849.
- (30) Pelliccia, D.; Nikulin, A. Y.; Muddle, B. C.; Sakata, O. *Scr. Mater.* **2011**, 64, 613.

- (31) Beyerlein, K. R.; Solla-Gullon, J.; Herrero, E.; Garnier, E.; Pailloux, F.; Leoni, M.; Scardi, P.; Snyder, R. L.; Aldaz, A.; Feliu, J. M. *Mater. Sci. Eng., A* **2010**, 528, 83.
- (32) Vogel, W.; He, W.; Huang, Q. H.; Zou, Z. Q.; Zhang, X. G.; Yang, H. *Int. J. Hydrogen Energy* **2010**, 35, 8609.
- (33) Malis, O.; Radu, M.; Mott, D.; Wanjala, B.; Luo, J.; Zhong, C. J. *Nanotechnology* **2009**, 20, 245708.
- (34) Kumpf, C. *Appl. Phys. A* **2006**, 85, 337.
- (35) Yan, W. F.; Petkov, V.; Mahurin, S. M.; Overbury, S. H.; Dai, S. *Catal. Commun.* **2005**, 6, 404.
- (36) Lee, K. M.; Lee, D. J.; Ahn, H. *Mater. Lett.* **2004**, 58, 3122.
- (37) Zhang, P.; Sham, T. K. *Phys. Rev. Lett.* **2003**, 90, 245502.
- (38) Sun, X. C.; Reyes-Gasga, J.; Dong, X. L. *Mol. Phys.* **2002**, 100, 3147.
- (39) Westesen, K.; Siekmann, B.; Koch, M. H. J. *Int. J. Pharm.* **1993**, 93, 189.
- (40) Avadhut, Y. S.; Weber, J.; Hammarberg, E.; Feldmann, C.; Schellenberg, I.; Pottgen, R.; der Gunne, J. S. A. *Chem. Mat.* **2011**, 23, 1526.
- (41) Verkuijlen, M. H. W.; Gao, J. B.; Adelhelm, P.; van Bentum, P. J. N.; de Jongh, P. E.; Kentgens, A. P. M. *J. Phys. Chem. C* **2010**, 114, 4683.
- (42) Grunberg, A.; Xu, Y. P.; Breitzke, H.; Buntkowsky, G. *Chem. Eur. J.* **2010**, 16, 6993.
- (43) Gervais, C.; Smith, M. E.; Pottier, A.; Jolivet, J. P.; Babonneau, F. *Chem. Mat.* **2001**, 13, 462.
- (44) Sreeja, V.; Smitha, T. S.; Nand, D.; Ajithkumar, T. G.; Joy, P. A. *J. Phys. Chem. C* **2008**, 112, 14737.

- (45) Sepelak, V.; Bergmann, I.; Indris, S.; Feldhoff, A.; Hahn, H.; Becker, K. D.; Grey, C. P.; Heitjans, P. *J. Mat. Chem.* **2011**, *21*, 8332.
- (46) Alam, T. M. *Mater. Chem. Phys.* **2004**, *85*, 310.
- (47) Jager, C.; Welzel, T.; Meyer-Zaika, W.; Epple, M. *Magn. Reson. Chem.* **2006**, *44*, 573.
- (48) Avolio, R.; Gentile, G.; Avella, M.; Capitani, D.; Errico, M. E. *J. Polym. Sci., Part A: Polym. Chem.* **2010**, *48*, 5618.
- (49) Sepelak, V.; Becker, K. D.; Bergmann, I.; Suzuki, S.; Indris, S.; Feldhoff, A.; Heitjans, P.; Grey, C. P. *Chem. Mat.* **2009**, *21*, 2518.
- (50) Berrettini, M. G.; Braun, G.; Hu, J. G.; Strouse, G. F. *J. Am. Chem. Soc.* **2004**, *126*, 7063.
- (51) O'Connor, R. D.; Zhang, Q.; Wooley, K. L.; Schaefer, J. *Helv. Chim. Acta* **2002**, *85*, 3219.
- (52) Ratcliffe, C. I.; Yu, K.; Ripmeester, J. A.; Zaman, M. B.; Badarau, C.; Singh, S. *Phys. Chem. Chem. Phys.* **2006**, *8*, 3510.
- (53) Novio, F.; Philippot, K.; Chaudret, B. *Catal. Lett.* **2010**, *140*, 1.
- (54) Mallisery, S. K.; Gudat, D. *Dalton Trans.* **2010**, *39*, 4280.
- (55) Fiurasek, P.; Reven, L. *Langmuir* **2007**, *23*, 2857.
- (56) Giuliani, J. R.; Harley, S. J.; Carter, R. S.; Power, P. P.; Augustine, M. P. *Solid State Nucl. Magn. Reson.* **2007**, *32*, 1.
- (57) de Monredon, S.; Cellot, A.; Ribot, F.; Sanchez, C.; Armelao, L.; Gueneau, L.; Delattre, L. *J. Mat. Chem.* **2002**, *12*, 2396.
- (58) Lo, A. Y. H.; Sudarsan, V.; Sivakumar, S.; van Veggel, F.; Schurko, R. W. *J. Am. Chem. Soc.* **2007**, *129*, 4687.

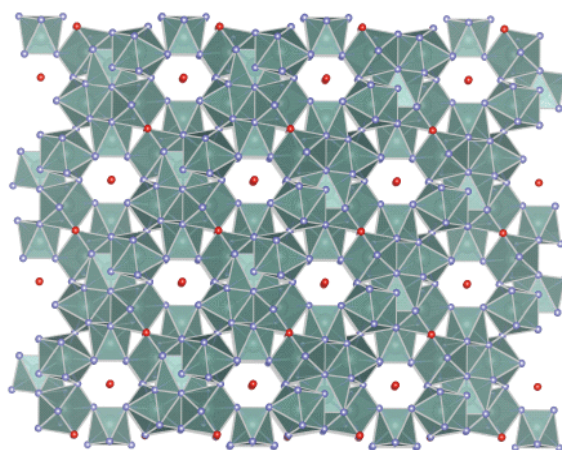
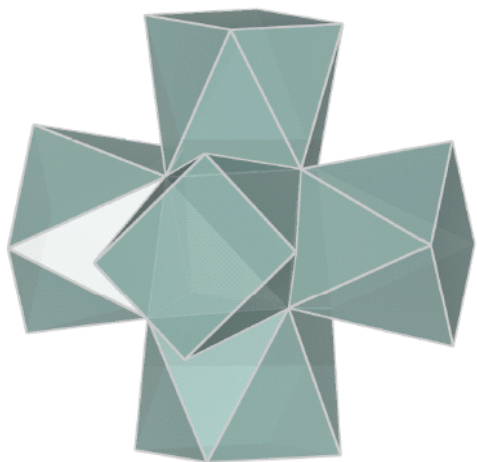
- (59) Reyes-Garcia, E. A.; Sun, Y. P.; Reyes-Gil, K.; Raftery, D. *J. Phys. Chem. C* **2007**, *111*, 2738.
- (60) Reyes-Garcia, E. A.; Sun, Y. P.; Reyes-Gil, K. R.; Raftery, D. *Solid State Nucl. Magn. Reson.* **2009**, *35*, 74.
- (61) Duan, X. L.; Yuan, D. R.; Yu, F. P. *Inorg. Chem.* **2011**, *50*, 5460.
- (62) Dolbier, W. R., Ed. *Guide to Fluorine NMR for Organic Chemists*; Wiley: Hoboken, NJ, 2009.
- (63) Miller, J. M. *Prog. Nucl. Magn. Reson. Spectrosc.* **1996**, *28*, 255.
- (64) MacKenzie, K. J. D.; Smith, M. E. *Multinuclear Solid-State NMR of Inorganic Materials*; Pergamon Press: Oxford, 2002.
- (65) Zalkin, A.; Templeton, D. H. *J. Am. Chem. Soc.* **1953**, *75*, 2453.
- (66) Kraus, W.; Nolze, G., Powdercell, v. 2.4, Federal Institute for Materials Research and Testing: Berlin, Germany, 2000.
- (67) Rietveld, H. *J. Appl. Crystallogr.* **1969**, *2*, 65.
- (68) Rodriguez-Carvajal, J. *Physica B* **1993**, *192*, 55.
- (69) Rodriguez-Carvajal, J. *J. Commission on Powder Diffraction (IUCr) Newsletter* **2001**, *26*, 12.
- (70) Thompson, P.; Cox, D. E.; Hastings, J. B. *J. Appl. Crystallogr.* **1987**, *20*, 79.
- (71) Momma, K.; Izumi, F. *J. Appl. Crystallogr.* **2011**, *44*, 1272.
- (72) Pines, A.; Gibby, M. G.; Waugh, J. S. *J. Chem. Phys.* **1973**, *59*, 569.
- (73) Peersen, O. B.; Wu, X.; Kustanovich, I.; Smith, S. O. *J. Magn. Reson., Ser. A* **1993**, *104*, 334.
- (74) Peersen, O. B.; Wu, X.; Smith, S. O. *J. Magn. Reson., Ser. A* **1994**, *106*, 127.

- (75) Bennett, A. E.; Rienstra, C. M.; Auger, M.; Lakshmi, K. V.; Griffin, R. G. *J. Chem. Phys.* **1995**, *103*, 6951.
- (76) Eichele, K.; Wasylishen, R. E., WSolid1: Solid-State NMR Spectrum Simulation, version 1.17.30, University of Tübingen, Tübingen, Germany, 2001.
- (77) Maguer, J. J.; Crosnier-Lopez, M. P.; Courbion, G. *J. Solid State Chem.* **1997**, *128*, 42.
- (78) Le Berre, F.; Boucher, E.; Allain, M.; Courbion, G. *J. Mat. Chem.* **2000**, *10*, 2578.
- (79) Stephens, N. F.; Lightfoot, P. *J. Solid State Chem.* **2007**, *180*, 260.
- (80) Maguer, J. J.; Courbion, G. *J. Solid State Chem.* **1997**, *128*, 52.
- (81) Trebosc, J.; Wiench, J. W.; Huh, S.; Lin, V. S. Y.; Pruski, M. *J. Am. Chem. Soc.* **2005**, *127*, 3057.
- (82) Grunberg, B.; Emmler, T.; Gedat, E.; Shenderovich, I.; Findenegg, G. H.; Limbach, H. H.; Buntkowsky, G. *Chem. Eur. J.* **2004**, *10*, 5689.
- (83) Crocker, M.; Herold, R. H. M.; Wilson, A. E.; Mackay, M.; Emeis, C. A.; Hoogendoorn, A. *M. J. Chem. Soc., Faraday Trans.* **1996**, *92*, 2791.
- (84) Hunger, M.; Freude, D.; Pfeifer, H. *J. Chem. Soc., Faraday Trans.* **1991**, *87*, 657.
- (85) Sheih, P. S.; Fendler, J. H. *J. Chem. Soc., Faraday Trans. 1* **1977**, *73*, 1480.
- (86) Demarco, A.; Menegatti, E.; Luisi, P. L. *J. Biochem. Bioph. Methods* **1986**, *12*, 325.
- (87) Law, S. J.; Britton, M. M. *Langmuir* **2012**, *28*, 11699.
- (88) Schneider, W. G.; Bernstein, H. J.; Pople, J. A. *J. Chem. Phys.* **1958**, *28*, 601.
- (89) Hindman, J. C. *J. Chem. Phys.* **1966**, *44*, 4582.
- (90) Lyons, D. M.; McGrath, J. P.; Morris, M. A. *J. Phys. Chem. B* **2003**, *107*, 4607.
- (91) Huittinen, N.; Sarv, P.; Lehto, J. *J. Colloid Interface Sci.* **2011**, *361*, 252.

- (92) Herzfeld, J.; Berger, A. E. *J. Chem. Phys.* **1980**, 73, 6021.
- (93) Simonov, V. I.; Bukvetsky, B. V. *Acta Crystallogr., Sect. B: Struct. Sci* **1978**, 34, 355.
- (94) Pines, A.; Waugh, J. S.; Gibby, M. G. *Chem. Phys. Lett.* **1972**, 15, 373.



## Table of Contents Graphic



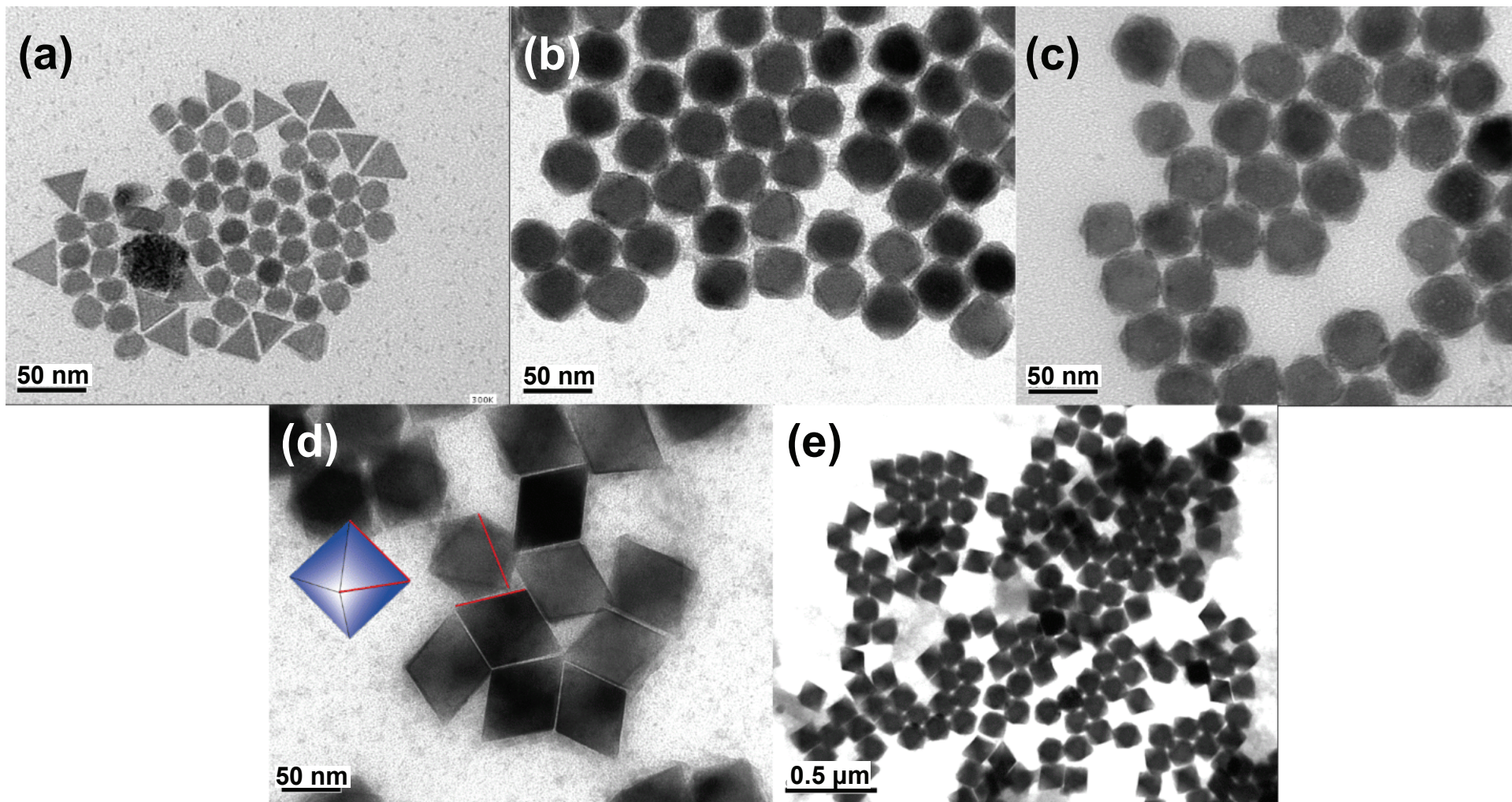


**Figure 1.** TEM images of octahedrally-shaped  $(\text{H}_3\text{O})\text{Y}_3\text{F}_{10} \cdot x\text{H}_2\text{O}$  nanoparticles, with a measured edge length of (a) 21 nm, (b) 37 nm, (c) 49 nm, (d) 67 nm, and (e) 132 nm. Octahedron edges shown in (d) are highlighted to demonstrate NP measurements.

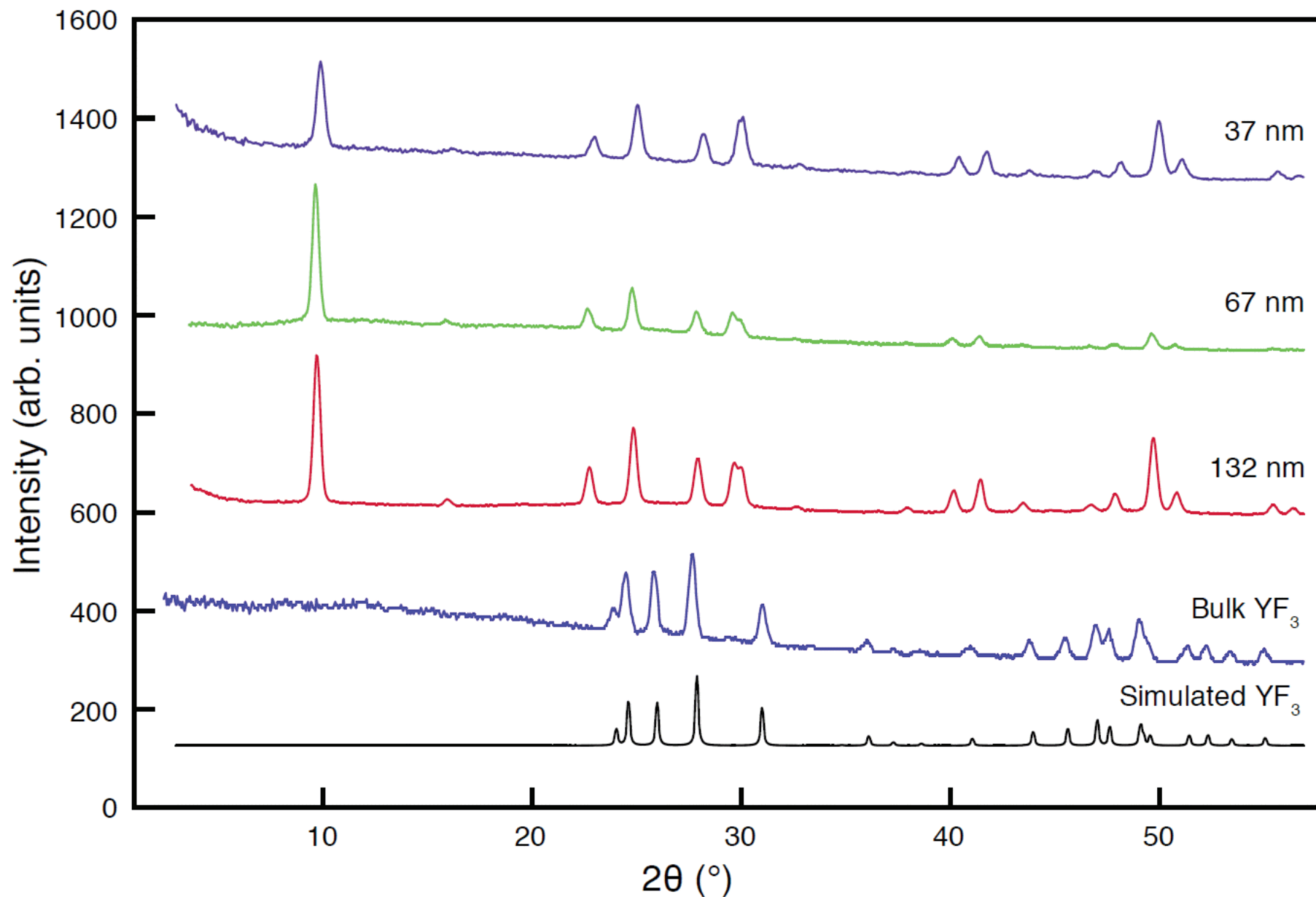


**Figure 2.** pXRD patterns collected for bulk YF<sub>3</sub> (space group *Pnma*) and (H<sub>3</sub>O)Y<sub>3</sub>F<sub>10</sub> • xH<sub>2</sub>O nanoparticles, (space group *Fd-3m*), with nanoparticle diameters listed in nm. A simulated pXRD pattern for bulk YF<sub>3</sub> is displayed at the bottom.

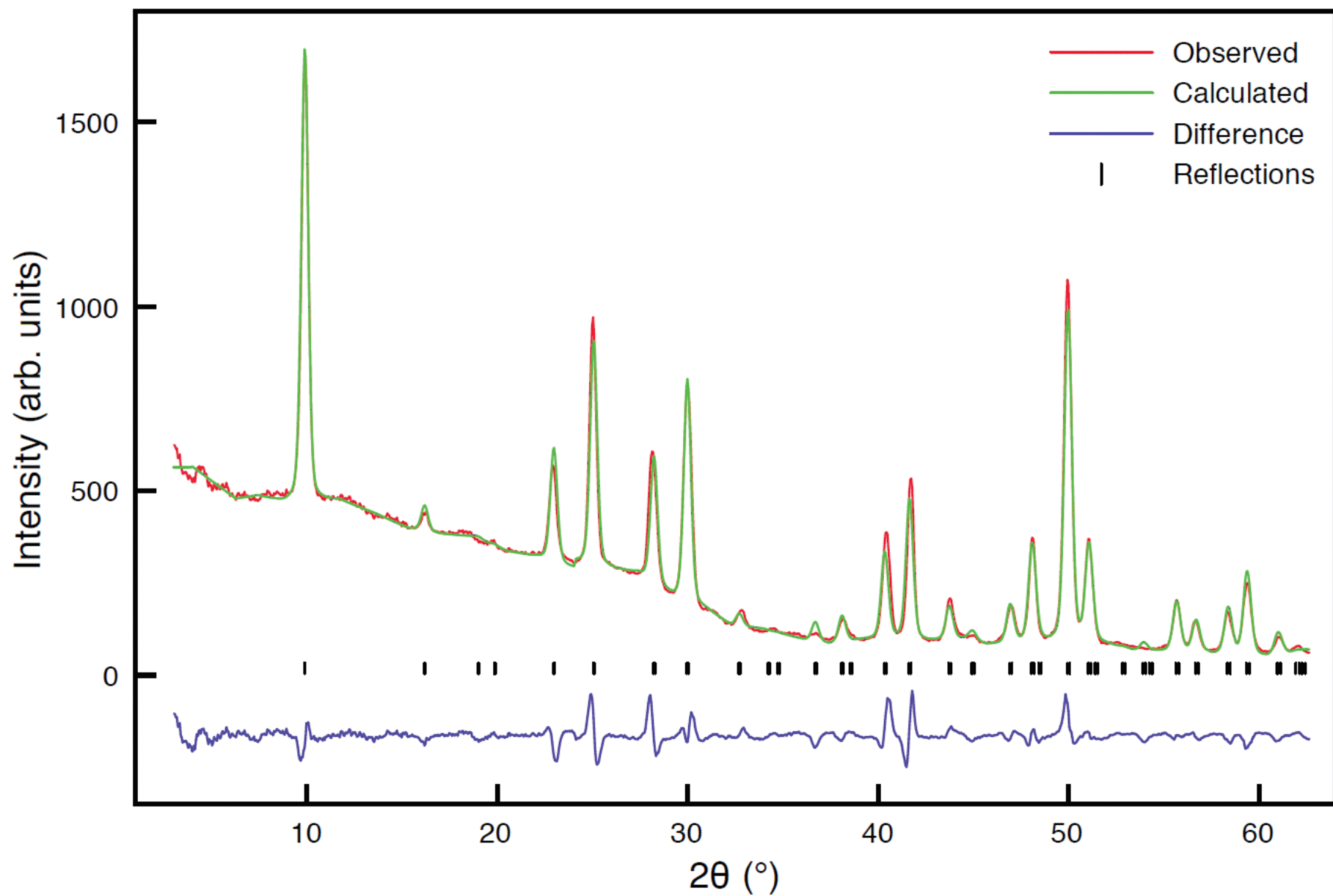


**Figure 3.** Rietveld profile for the 67 nm diameter  $(\text{H}_3\text{O})\text{Y}_3\text{F}_{10} \cdot x\text{H}_2\text{O}$  nanoparticles using the space group  $Fd-3m$ .



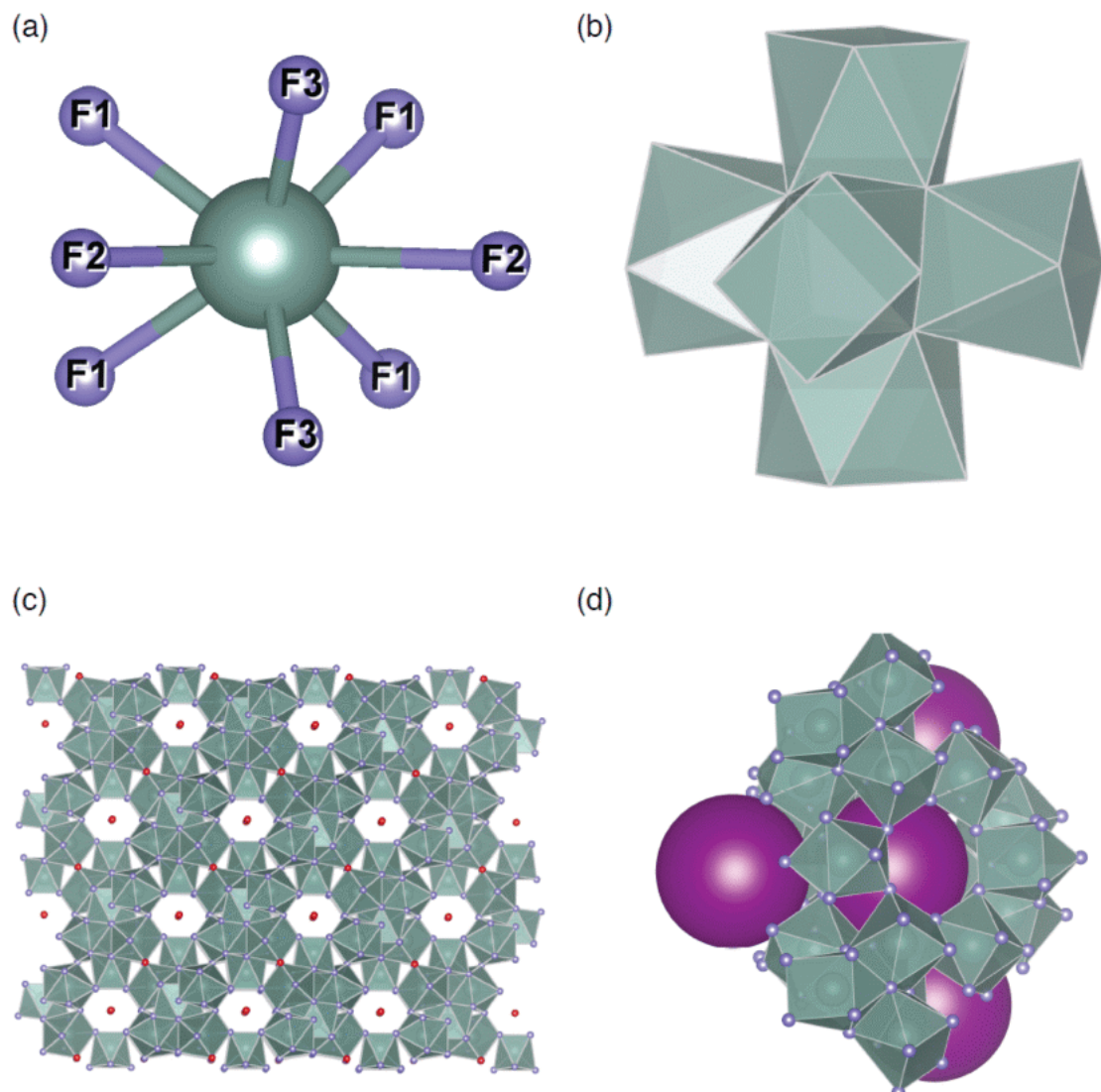


**Figure 4.** Schematic representation of the  $(\text{H}_3\text{O})\text{Y}_3\text{F}_{10} \cdot x\text{H}_2\text{O}$  diamond-like structure where (a) represents the  $\text{YF}_8$  coordination polyhedra, (b) represents the  $[\text{Y}_6\text{F}_{32}]^{14-}$  UOA octahedral-like building units, (c) and (d) represent the cage like structure exhibited by the nanoparticles. Fluorine ions are denoted by blue spheres and the yttrium polyhedra are denoted in grey. In (c) the red spheres denote the oxygen ions associated with the  $\text{H}_3\text{O}^+$  moiety and in (d) the purple spheres indicate the void spaces. The positions of the water molecules within the cages are not shown.

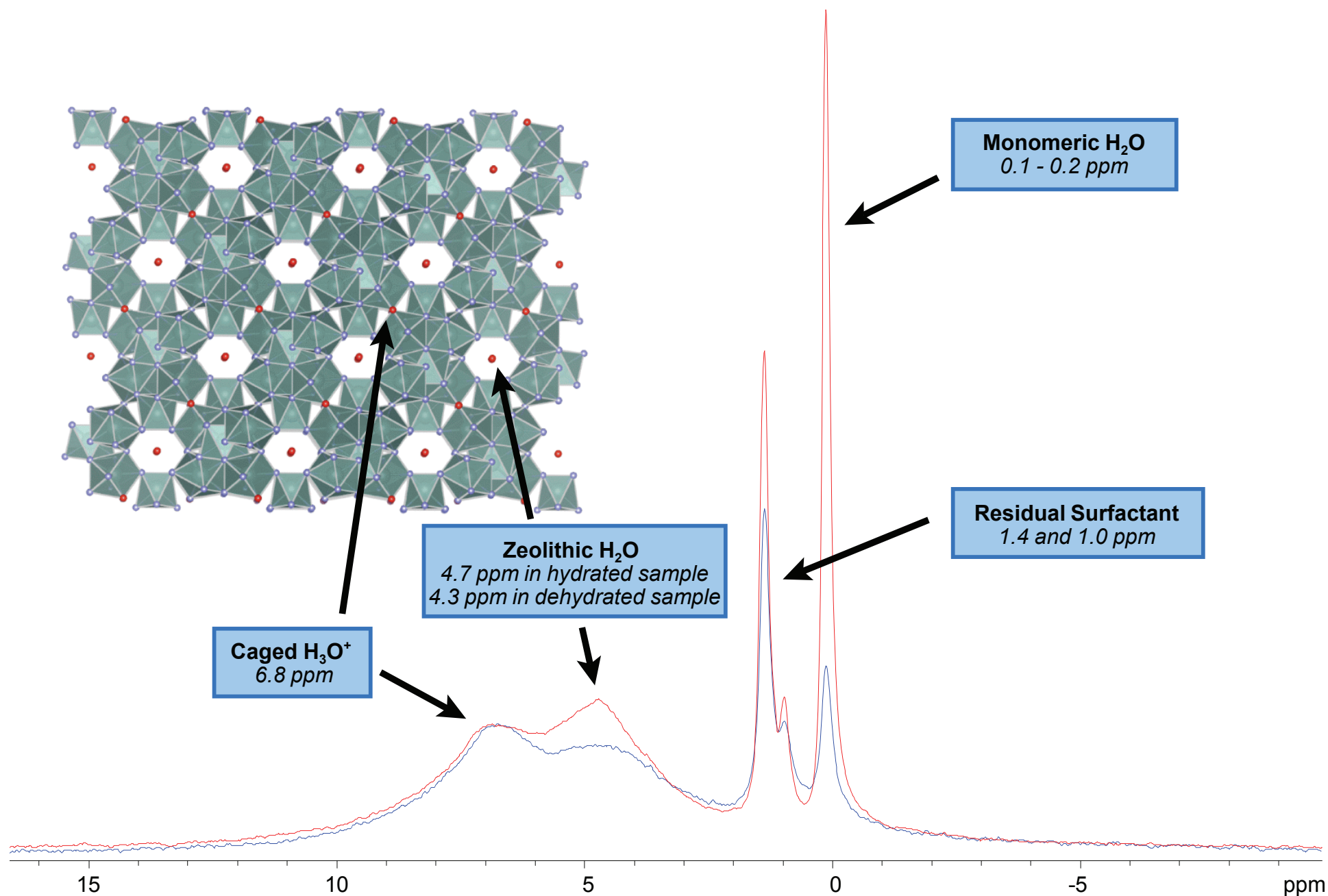


**Figure 5.**  $^1\text{H}$  MAS spectra of 67 nm  $(\text{H}_3\text{O})\text{Y}_3\text{F}_{10} \cdot x\text{H}_2\text{O}$  nanoparticles at a spinning speed of 25 kHz. The red trace corresponds to a fully hydrated ( $x = 1$ ) sample, and the blue trace corresponds to a partially hydrated ( $x < 1$ ) sample. Inset left:  $(\text{H}_3\text{O})\text{Y}_3\text{F}_{10} \cdot x\text{H}_2\text{O}$  crystal structure.

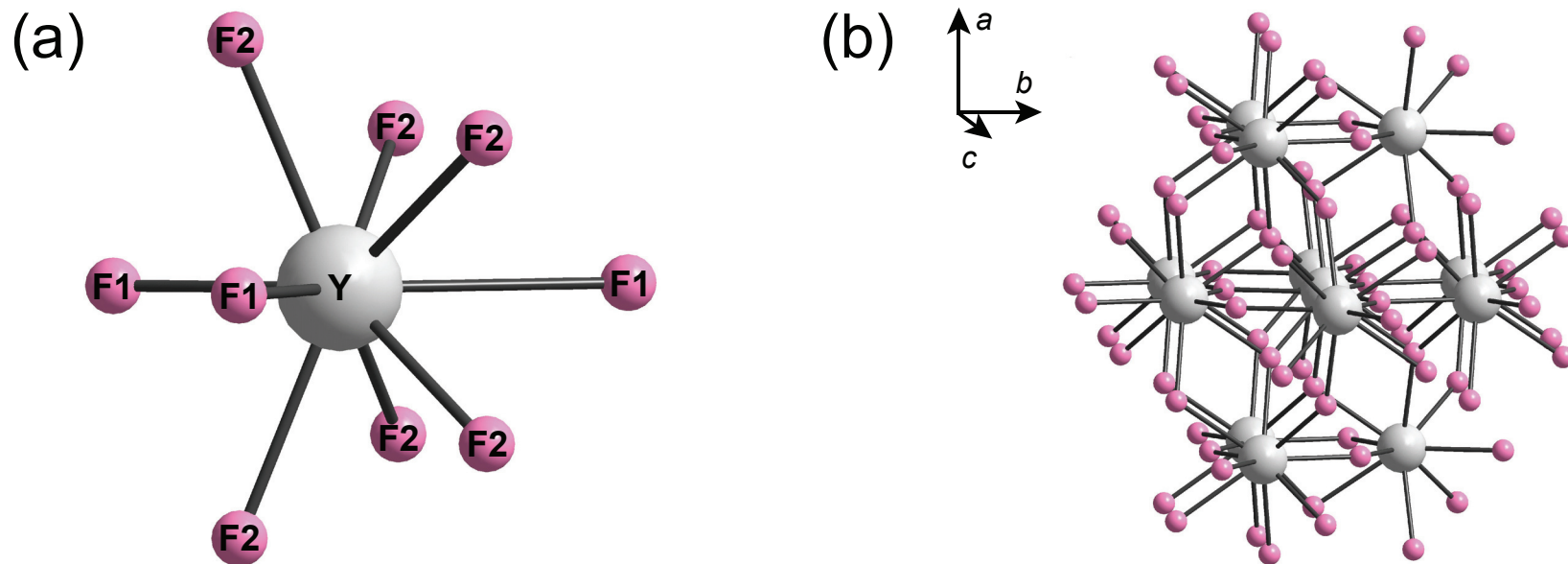


**Figure 6.** (a) The local nine-coordinate environment about yttrium and (b) the extended structure of bulk  $\text{YF}_3$ . There are two fluorine sites in a 1:2 ratio and one unique yttrium center.

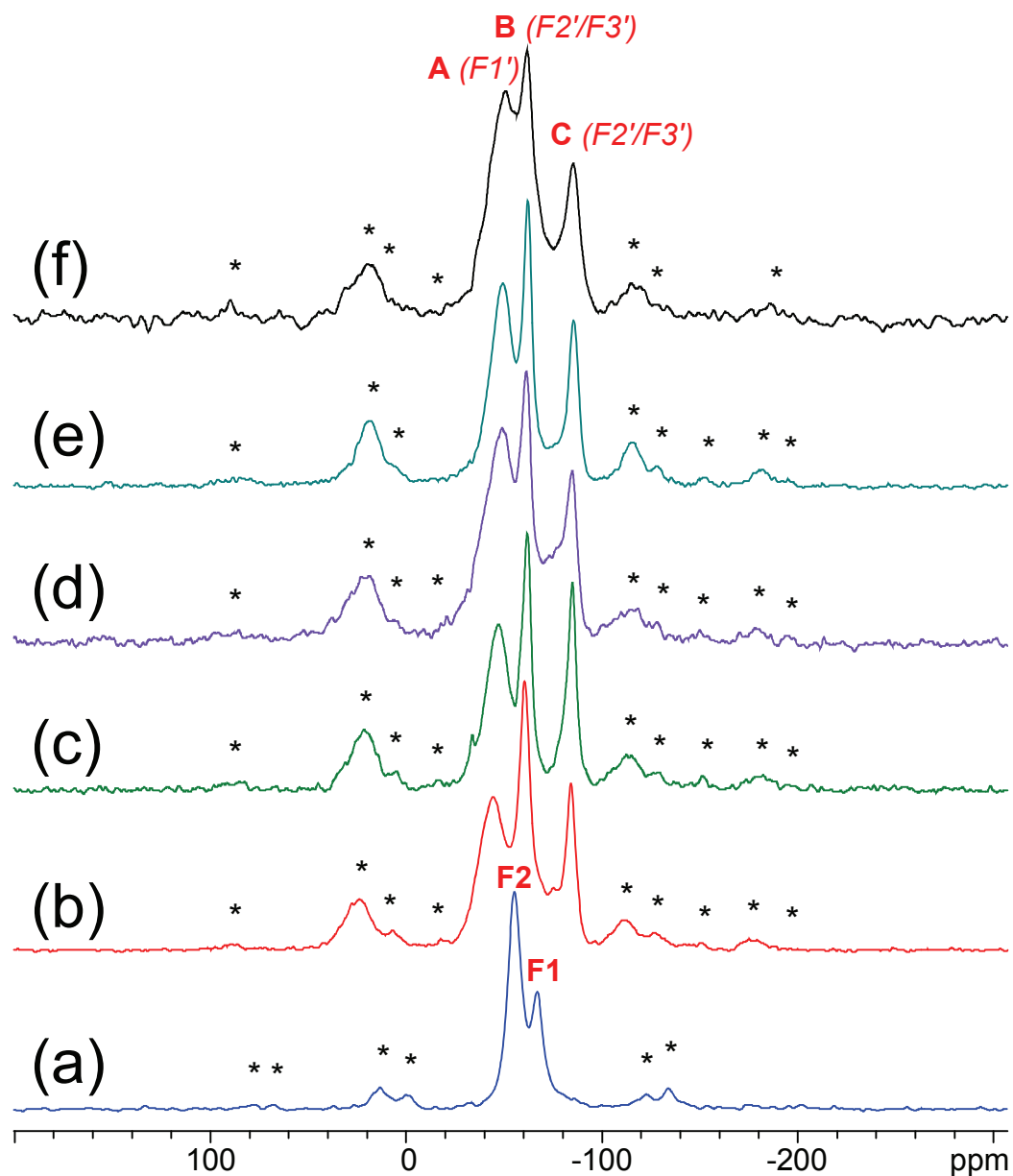


**Figure 7.**  $^{19}\text{F}$  MAS NMR spectra of (a) bulk  $\text{YF}_3$  and hydrated  $(\text{H}_3\text{O})\text{Y}_3\text{F}_{10} \cdot x\text{H}_2\text{O}$  nanoparticles of size (b) 132 nm, (c) 67 nm, (d) 49 nm, (e) 37 nm, and (f) 21 nm. Spectra recorded at a spinning speed of 25 kHz. F1 and F2 in (a) denote isotropic chemical shifts in bulk  $\text{YF}_3$ , A, B, and C for (b)-(f) denote isotropic chemical shifts in  $(\text{H}_3\text{O})\text{Y}_3\text{F}_{10} \cdot x\text{H}_2\text{O}$ , while asterisks (\*) denote spinning sidebands.



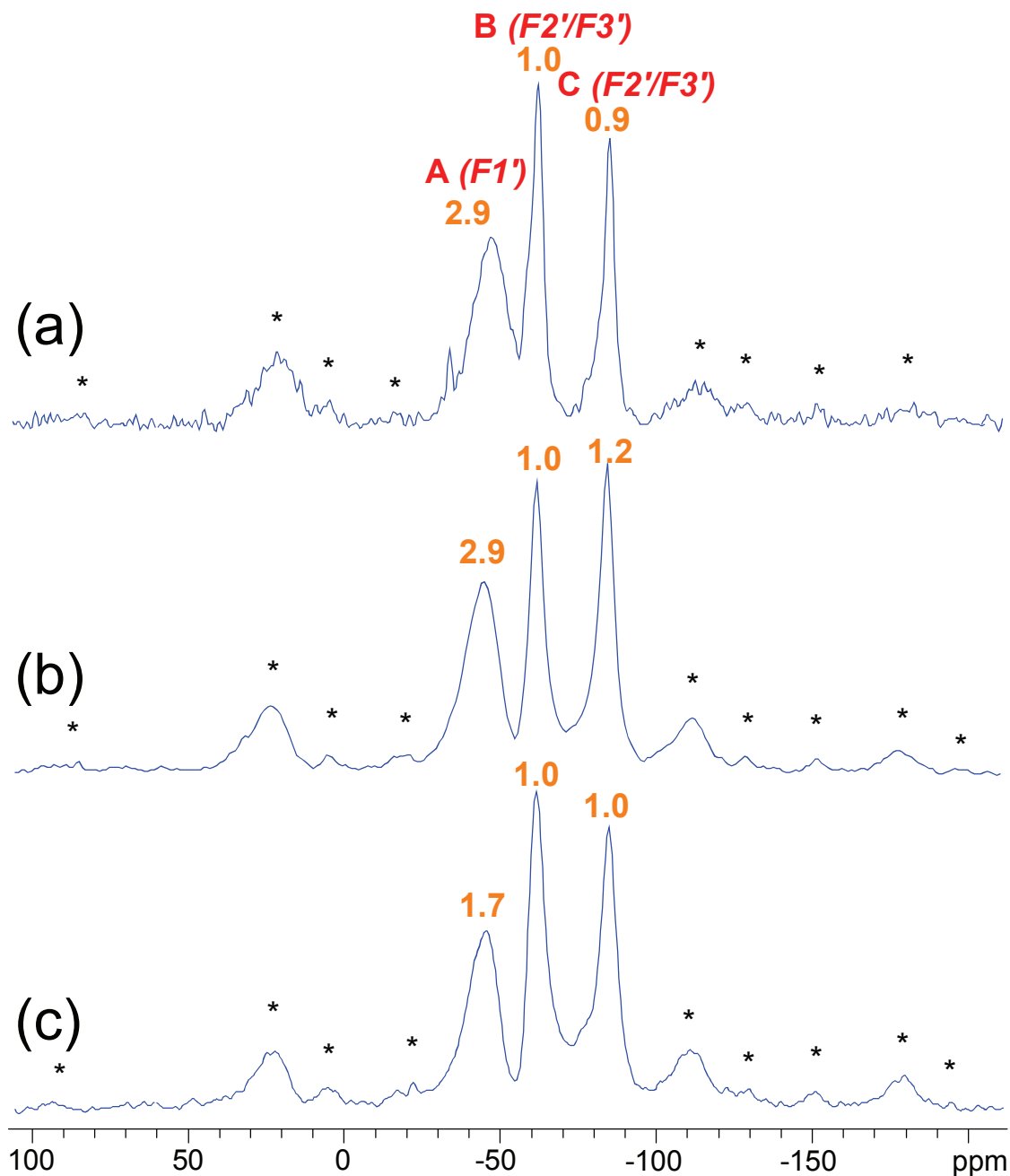


**Figure 8.**  $^{19}\text{F}$  MAS NMR spectra for 67 nm  $(\text{H}_3\text{O})\text{Y}_3\text{F}_{10} \cdot x\text{H}_2\text{O}$  nanoparticles (a) as received (hydrated), (b) after prolonged air exposure (hydrated), (c) after 12 hours of heating at 125 °C (partially hydrated). Spectra were recorded at a spinning speed of 25 kHz. Peak labels indicate resonance assignment and integration ratios (including spinning sidebands). Asterisks (\*) denote spinning sidebands.

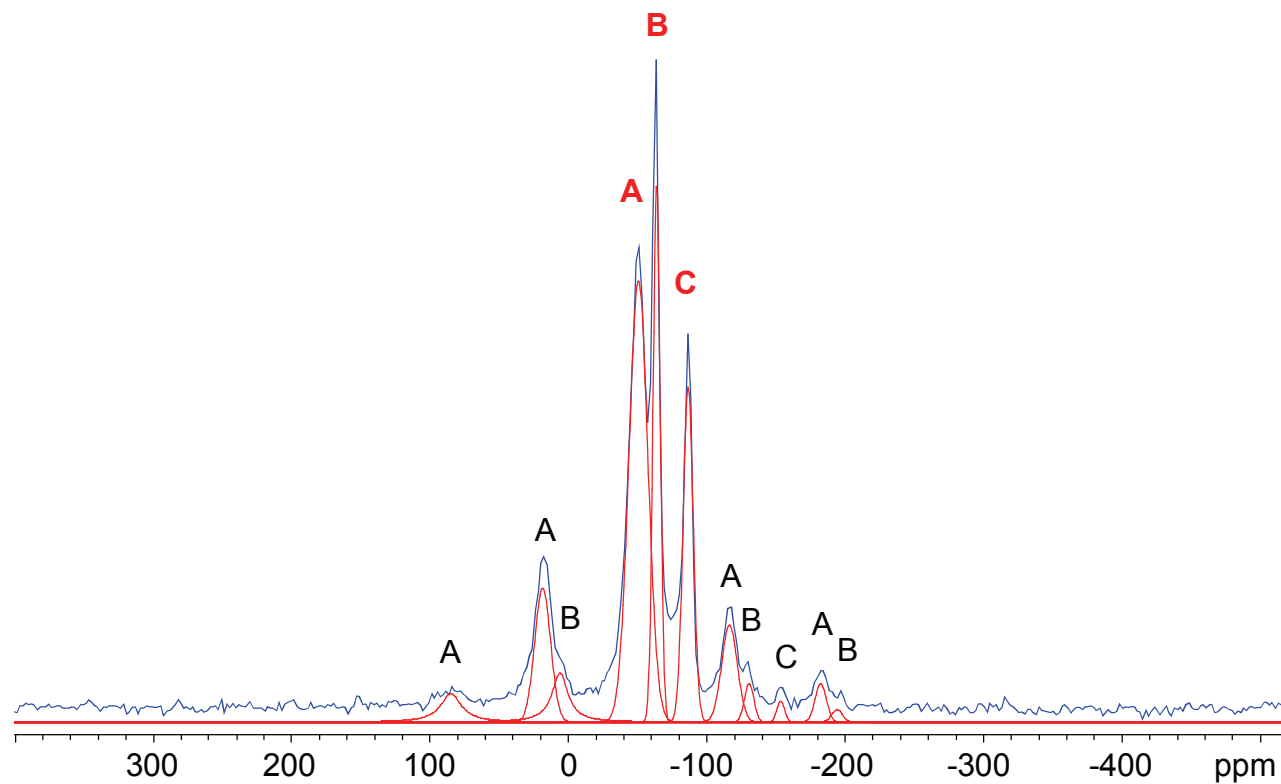


**Figure 9.** Deconvoluted  $^{19}\text{F}$  MAS NMR spectra of hydrated 37 nm  $(\text{H}_3\text{O})\text{Y}_3\text{F}_{10} \cdot x\text{H}_2\text{O}$  nanoparticles. Spinning sidebands are labeled according to the corresponding isotropic peak. Spectra were recorded at a spinning speed of 25 kHz.

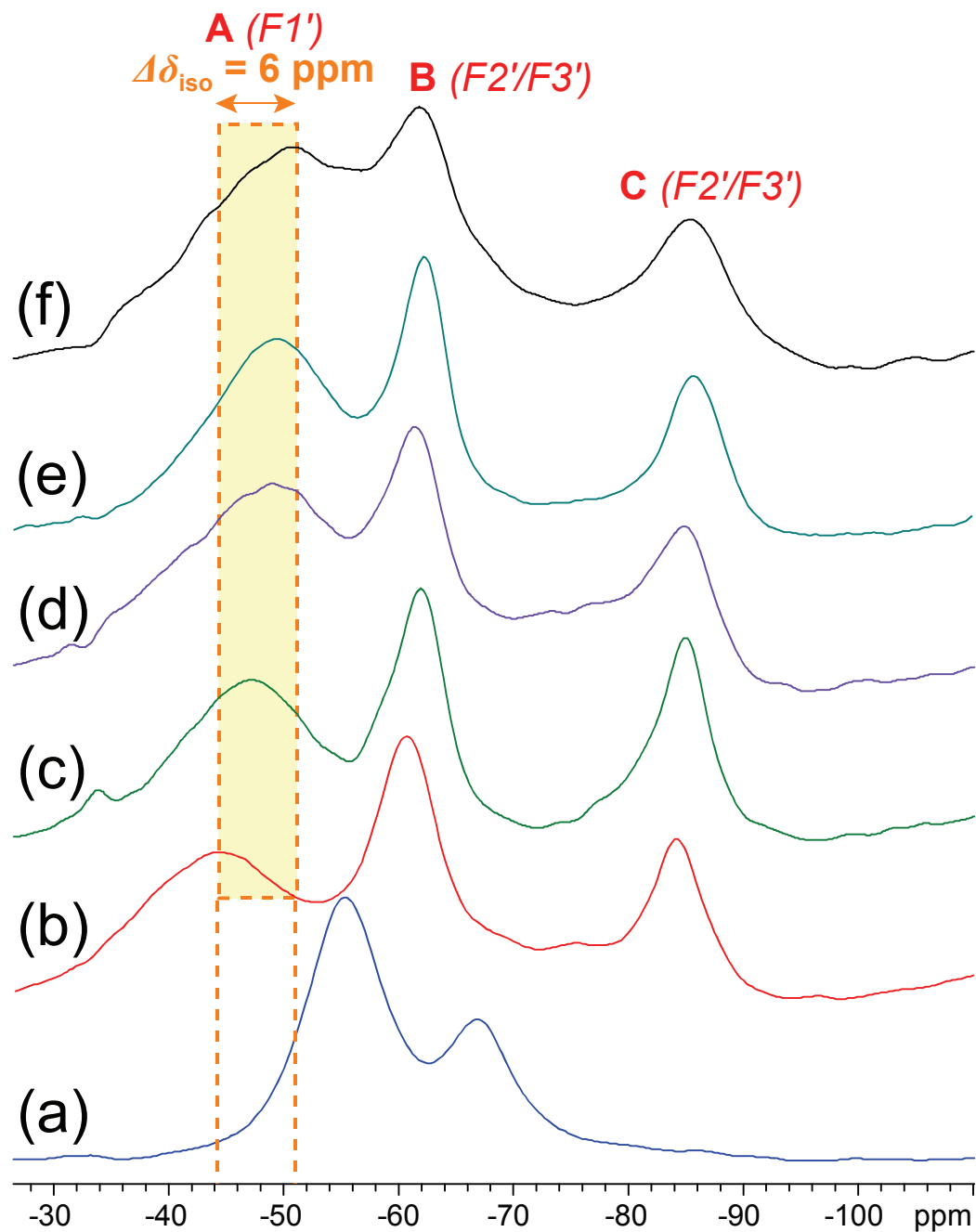


**Figure 10.** Change in  $\delta_{\text{iso}}$  of resonance A correlated with nanoparticle size in  $^{19}\text{F}$  MAS NMR spectra of hydrated  $(\text{H}_3\text{O})\text{Y}_3\text{F}_{10} \cdot x\text{H}_2\text{O}$  nanoparticles of size (b) 132 nm, (c) 67 nm, (d) 49 nm, (e) 37 nm, and (f) 21 nm. Bulk  $\text{YF}_3$  is shown in (a) for comparison. Spectra recorded at a spinning speed of 25 kHz. A, B, and C denote isotropic chemical shifts in hydrated  $(\text{H}_3\text{O})\text{Y}_3\text{F}_{10} \cdot x\text{H}_2\text{O}$ .

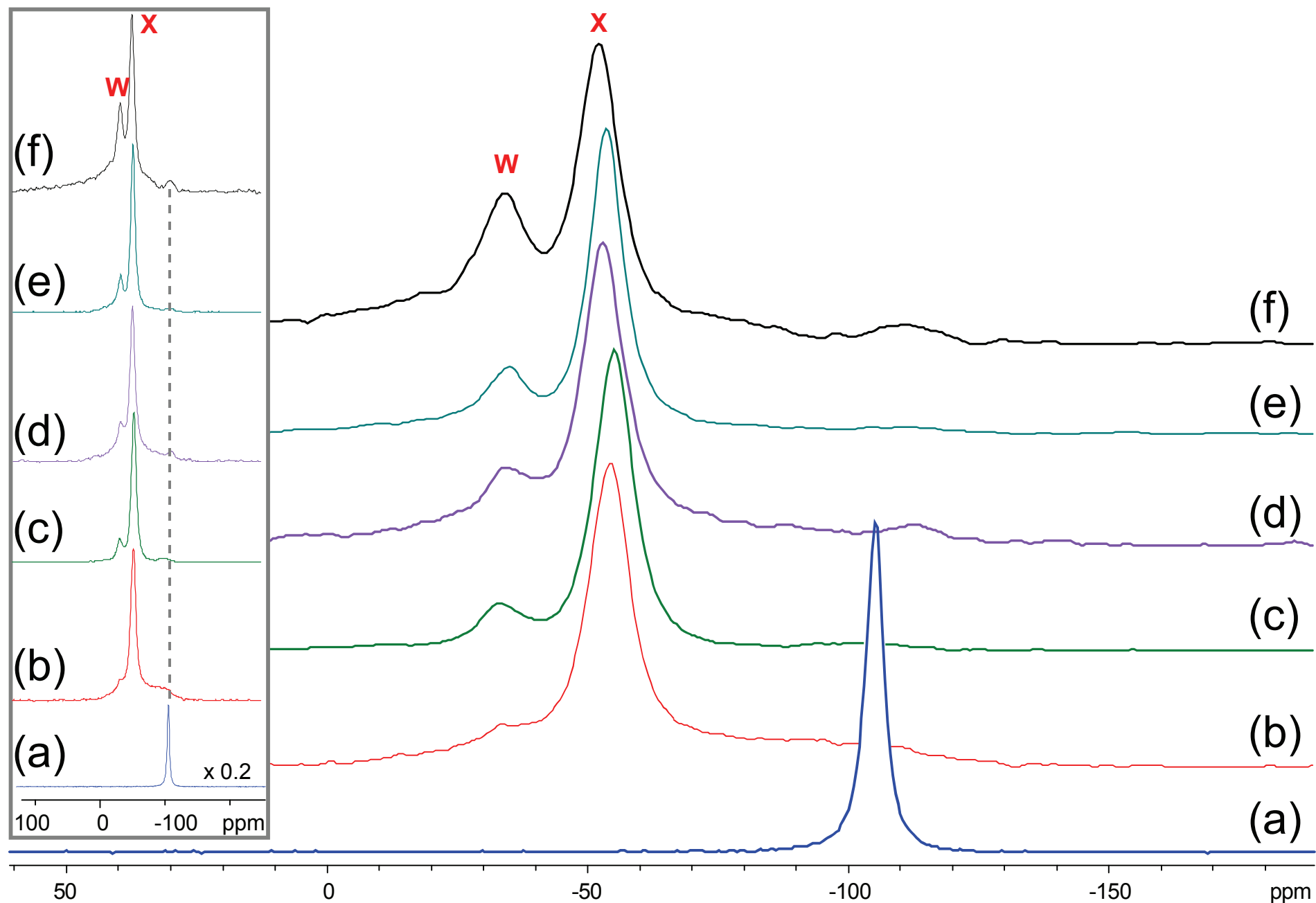


**Figure 11.**  $^{19}\text{F}$ - $^{89}\text{Y}$  VACP/MAS NMR spectra of bulk  $\text{YF}_3$  (a) and hydrated  $(\text{H}_3\text{O})\text{Y}_3\text{F}_{10} \cdot x\text{H}_2\text{O}$  nanoparticles of size (b) 132 nm, (c) 67 nm, (d) 49 nm, (e) 37 nm, and (f) 21 nm. Spectra recorded at a spinning speed of 5 kHz. Inset left: The dashed grey line indicates traces of bulk  $\text{YF}_3$  exist as various degrees of impurity in the  $(\text{H}_3\text{O})\text{Y}_3\text{F}_{10} \cdot x\text{H}_2\text{O}$  nanoparticle samples.

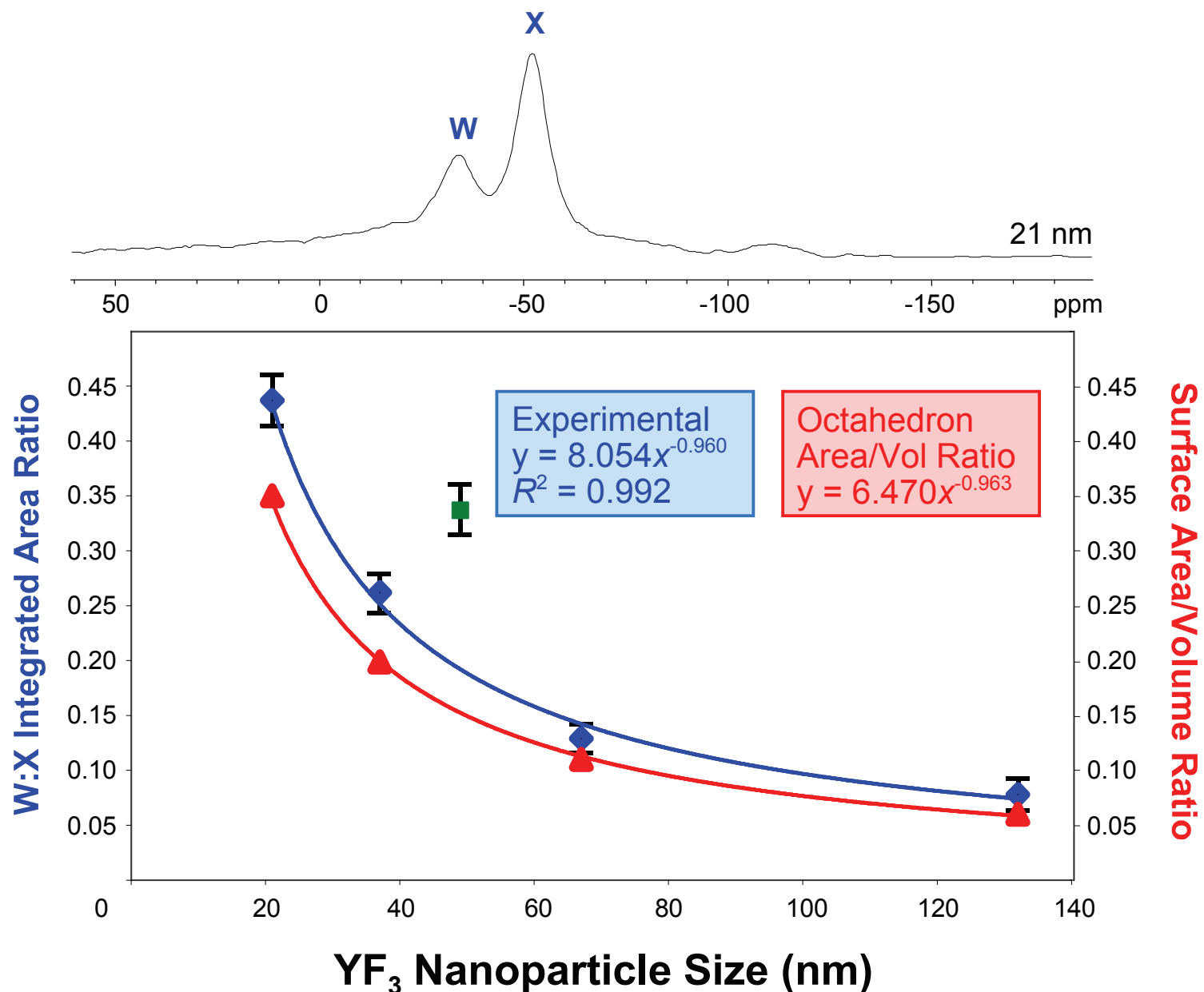


**Figure 12.** The graph depicts the relationship between the ratio of the integrated areas of **W** and **X** peaks and (H<sub>3</sub>O)Y<sub>3</sub>F<sub>10</sub> • xH<sub>2</sub>O NP size in <sup>19</sup>F-<sup>89</sup>Y VACP/MAS spectra of hydrated samples. Blue data points represent experimental ratios, red data points represent surface area/volume ratios of ideal octahedra (see Table 6). The green outlier represents the 49 nm Sc-doped (H<sub>3</sub>O)Y<sub>3</sub>F<sub>10</sub> • xH<sub>2</sub>O nanoparticles.

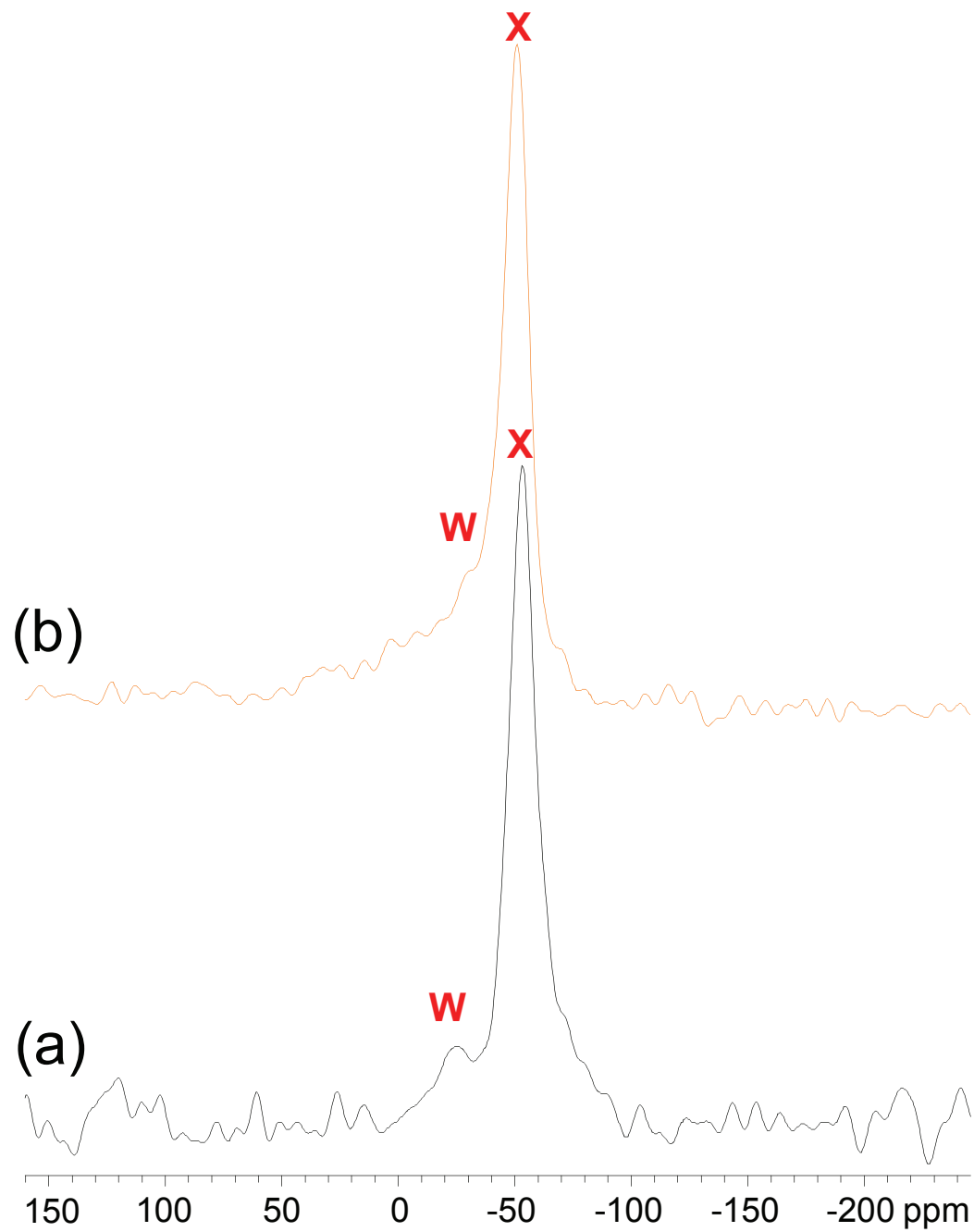


**Figure 13.**  $^{19}\text{F}$ - $^{89}\text{Y}$  VACP/MAS NMR spectra of 83 nm  $(\text{H}_3\text{O})\text{Y}_3\text{F}_{10} \cdot x\text{H}_2\text{O}$  nanoparticles, where (a) is a fully hydrated sample, and (b) is only partially hydrated. Spectra were recorded at a spinning speed of 5 kHz.

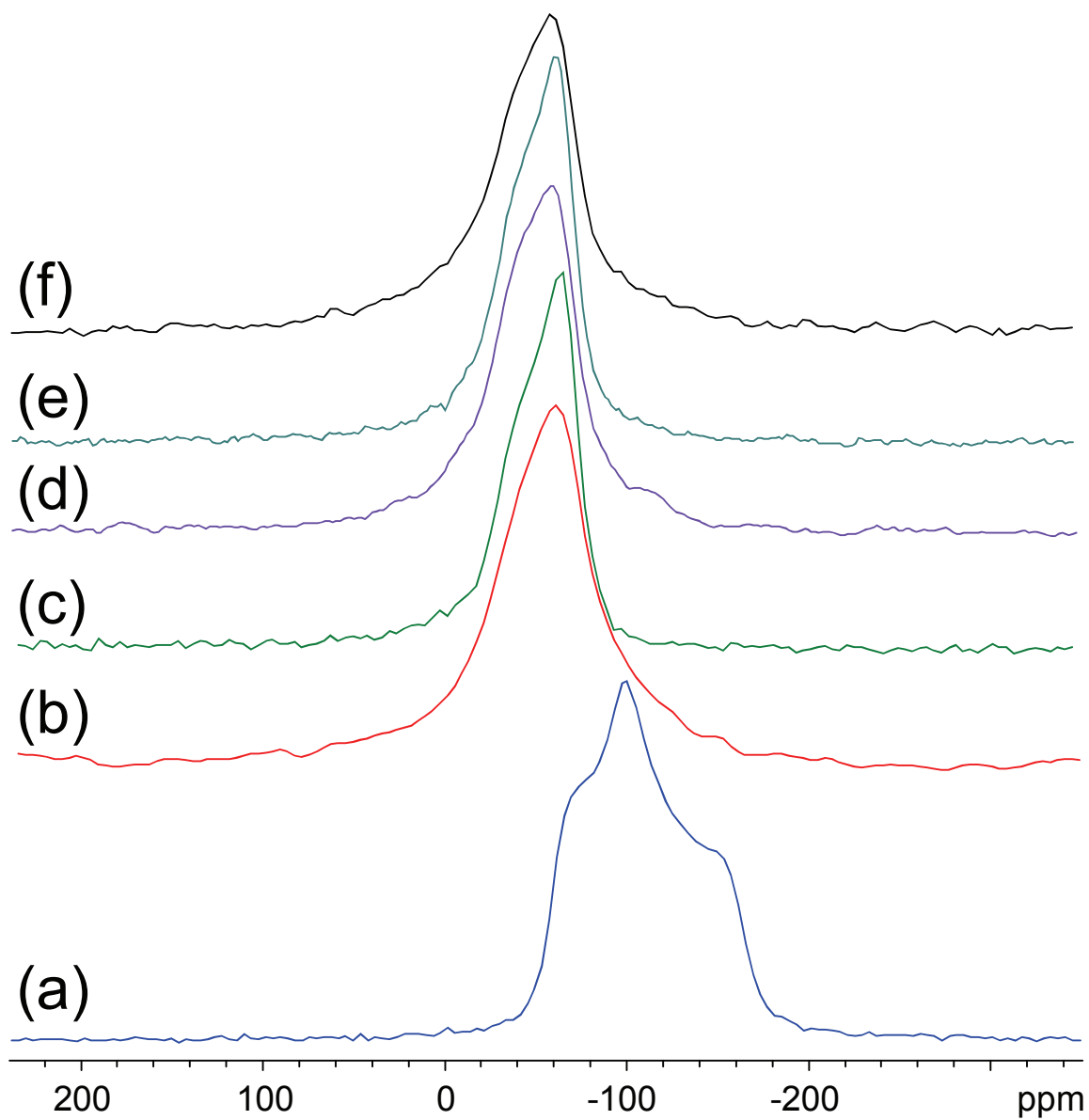


**Figure 14.** Static  $^{19}\text{F}$ - $^{89}\text{Y}$  VACP NMR spectra of (a) bulk  $\text{YF}_3$  and hydrated  $(\text{H}_3\text{O})\text{Y}_3\text{F}_{10} \cdot x\text{H}_2\text{O}$  nanoparticles of size (b) 132 nm, (c) 67 nm, (d) 49 nm, (e) 37 nm, and (f) 21 nm.

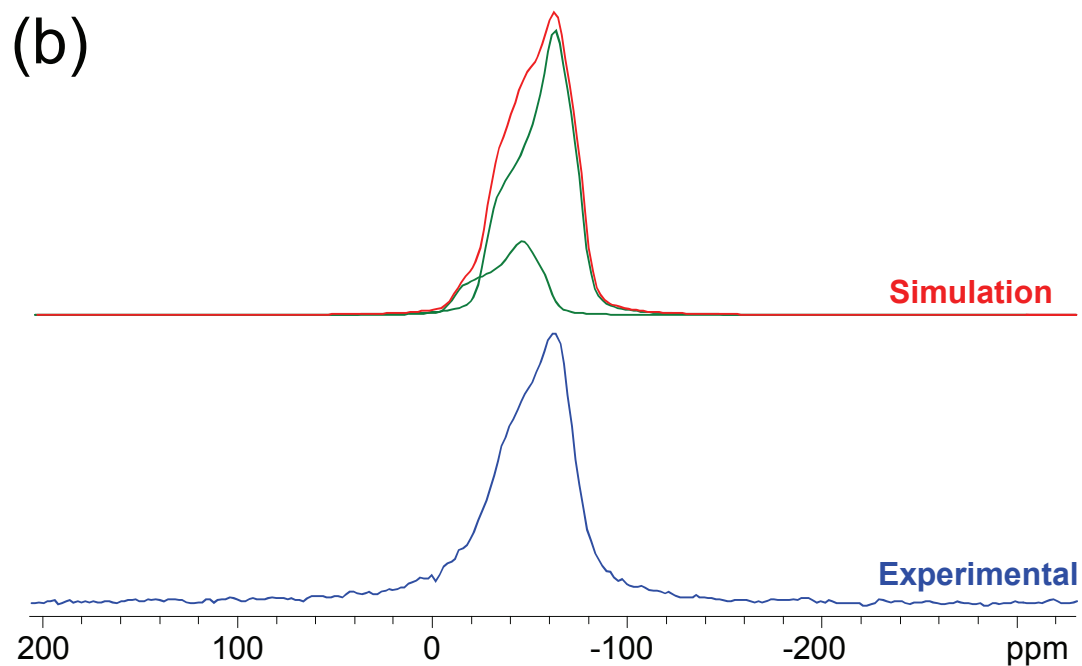
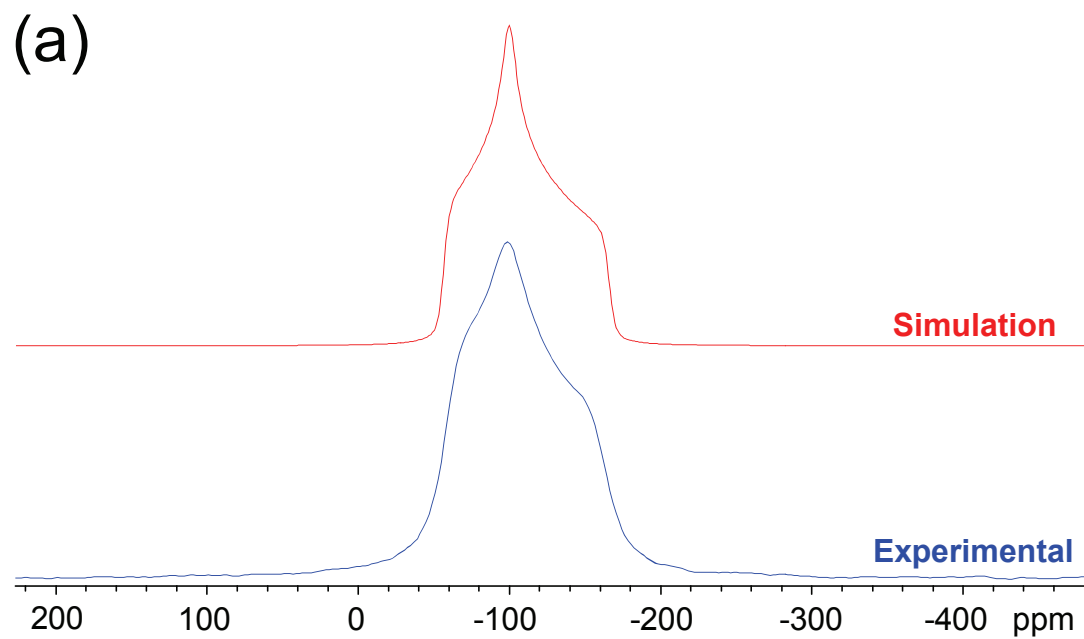


**Figure 15.** Static  $^{19}\text{F}$ - $^{89}\text{Y}$  VACP NMR spectra and simulation of (a) bulk  $\text{YF}_3$  and (b) hydrated 37 nm  $(\text{H}_3\text{O})\text{Y}_3\text{F}_{10} \cdot x\text{H}_2\text{O}$  nanoparticles. See Table 7.



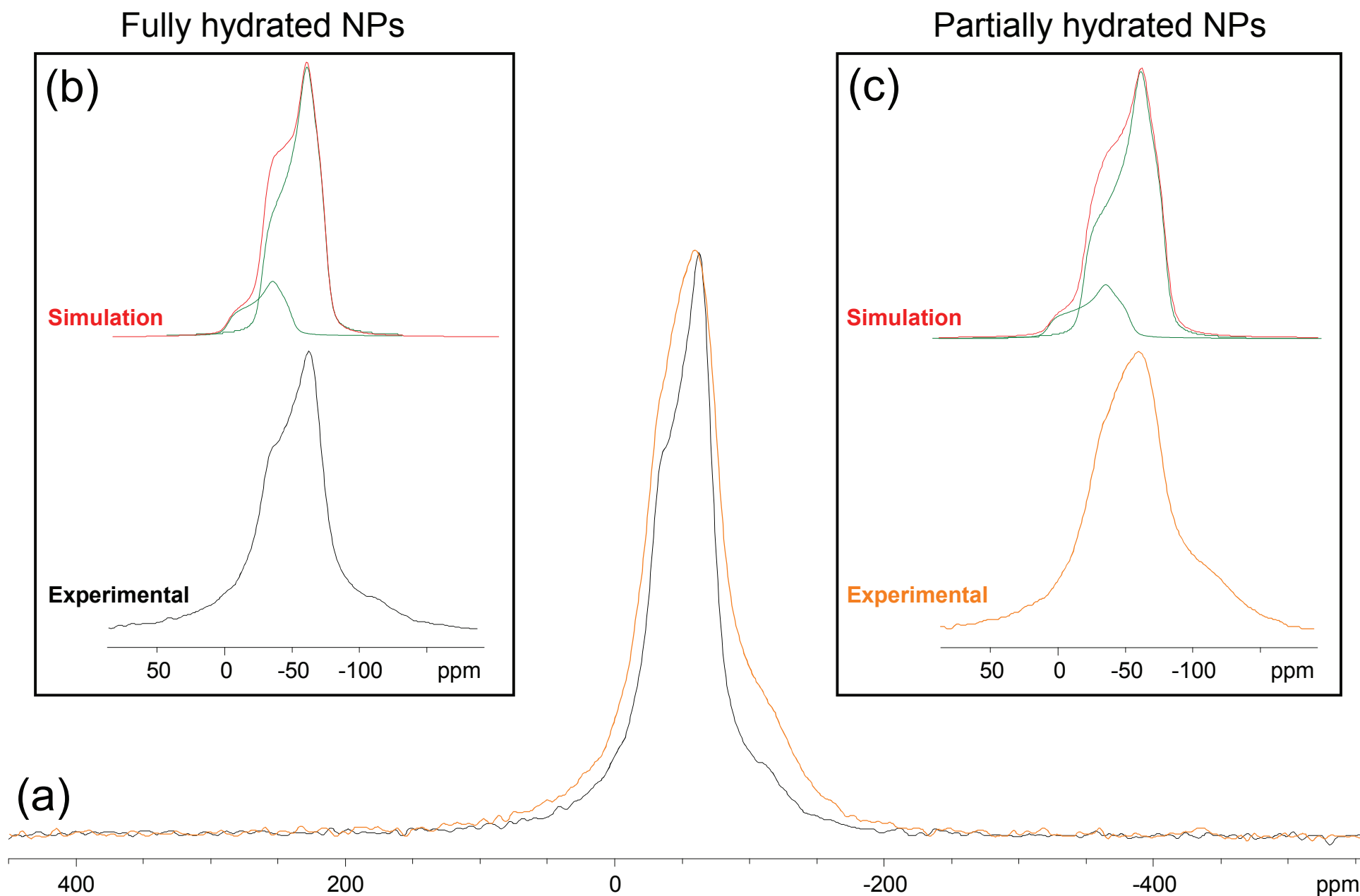


**Figure 16.** Overlaid static  $^{19}\text{F}$ - $^{89}\text{Y}$  VACP NMR spectra of fully (black) and partially (orange) hydrated 83 nm  $(\text{H}_3\text{O})\text{Y}_3\text{F}_{10} \cdot x\text{H}_2\text{O}$  nanoparticles are shown in (a). Simulations of spectra of the fully ((b), inset left), and partially ((c), inset right) hydrated NPs are also shown. See Table 7.